The ATLAS 3D project – XXIV. The intrinsic shape distribution of early-type galaxies

Anne-Marie Weijmans, P. de Zeeuw, Eric Emsellem, Davor Krajnović, Pierre-Yves Lablanche, Katherine Alatalo, Leo Blitz, Maxime Bois, Frédéric Bournaud, Martin Bureau, et al.

Mon. Not. R. Astron. Soc. **000**, 1–18 (2014) Printed 13 June 2021 (MN LATEX style file v2.2)

The ATLAS^{3D} project - XXIV. The intrinsic shape distribution of early-type galaxies

Anne-Marie Weijmans[1,2⋆†], P. T. de Zeeuw[3,4], Eric Emsellem[3,5], Davor Krajnović[6], Pierre-Yves Lablanche[5], Katherine Alatalo[7,8], Leo Blitz[7], Maxime Bois[9], Frédéric Bournaud[10], Martin Bureau[11], Michele Cappellari[11], Alison F. Crocker[12], Roger L. Davies[11], Timothy A. Davis[3], Pierre-Alain Duc[10], Sadegh Khochfar[13], Harald Kuntschner[3], Richard M. McDermid[14,15,16], Raffaella Morganti[17,18], Thorsten Naab[19], Tom Oosterloo[17,18], Marc Sarzi[20], Nicholas Scott[21], Paolo Serra[17,22], Gijs Verdoes Kleijn[18] & Lisa M. Young[23]

[1] *School of Physics and Astronomy, University of St Andrews, North Haugh, St Andrews KY16 9SS, UK*
[2] *Dunlap Institute for Astronomy & Astrophysics, University of Toronto, 50 St. George Street, Toronto, ON M5S 3H4, Canada*
[3] *European Southern Observatory, Karl-Schwarzschild-Str. 2, 85748 Garching, Germany*
[4] *Sterrewacht Leiden, Leiden University, Postbus 9513, 2300 RA Leiden, the Netherlands*
[5] *Université Lyon 1, Observatoire de Lyon, Centre de Recherche Astrophysique de Lyon and Ecole Normale Supérieure de Lyon, 9 avenue Charles André, F-69230 Saint-Genis Laval, France*
[6] *Leibniz-Institut für Astrophysik Potsdam (AIP), An der Sternwarte 16, D-14482 Potsdam, Germany*
[7] *Department of Astronomy, Campbell Hall, University of California, Berkeley, CA 94720, USA*
[8] *Infrared Processing and Analysis Center, California Institute of Technology, Pasadena, California 91125, USA*
[9] *Observatoire de Paris, LERMA and CNRS, 61 Av. de l'Observatoire, F-75014 Paris, France*
[10] *Laboratoire AIM Paris-Saclay, CEA/IRFU/SAp CNRS Université Paris Diderot, 91191 Gif-sur-Yvette Cedex, France*
[11] *Sub-department of Astrophysics, Department of Physics, University of Oxford, Denys Wilkinson Building, Keble Road, Oxford OX1 3RH*
[12] *Ritter Astrophysical Observatory, University of Toledo, Toledo, OH 43606, USA*
[13] *Institute for Astronomy, University of Edinburgh, Royal Observatory, Edinburgh EH9 3HJ, UK*
[14] *Gemini Observatory, Northern Operations Centre, 670 N. A'ohoku Place, Hilo, HI 96720, USA*
[15] *Department of Physics and Astronomy and MQ Research Centre in Astronomy, Astrophysics and Astrophotonics, Macquarie University, NSW 2109,*
[16] *Australian Astronomical Observatory, PO Box 296, NSW 1710, Australia*
[17] *Netherlands Institute for Radio Astronomy (ASTRON), Postbus 2, 7990 AA Dwingeloo, The Netherlands*
[18] *Kapteyn Astronomical Institute, University of Groningen, Postbus 800, 9700 AV Groningen, The Netherlands*
[19] *Max-Planck-Institut für Astrophysik, Karl-Schwarzschild-Str. 1, 85741 Garching, Germany*
[20] *Centre for Astrophysics Research, University of Hertfordshire, Hatfield, Herts AL1 9AB, UK*
[21] *Centre for Astrophysics and Supercomputing, Swinburne University of Technology, Hawthorn, Victoria 3122, Australia*
[22] *CSIRO Astronomy and Space Science, Australia Telescope National Facility, PO Box 76, Epping, NSW 1710, Australia*
[23] *Physics Department, New Mexico Institute of Mining and Technology, Socorro, NM 87801, USA*

13 June 2021

ABSTRACT

We use the ATLAS^{3D}sample to perform a study of the intrinsic shapes of early-type galaxies, taking advantage of the available combined photometric and kinematic data. Based on our ellipticity measurements from the Sloan Digital Sky Survey Data Release 7, and additional imaging from the Isaac Newton Telescope, we first invert the shape distribution of fast and slow rotators under the assumption of axisymmetry. The so-obtained intrinsic shape distribution for the fast rotators can be described with a Gaussian with a mean flattening of $q = 0.25$ and standard deviation $\sigma_q = 0.14$, and an additional tail towards rounder shapes. The slow rotators are much rounder, and are well described with a Gaussian with mean $q = 0.63$ and $\sigma_q = 0.09$. We then checked that our results were consistent when applying a different and independent method to obtain intrinsic shape distributions, by fitting the observed ellipticity distributions directly using Gaussian parametrisations for the intrinsic axis ratios. Although both fast and slow rotators are identified as early-type galaxies in morphological studies, and in many previous shape studies are therefore grouped together, their shape distributions are significantly different, hinting at different formation scenarios. The intrinsic shape distribution of the fast rotators shows similarities with the spiral galaxy population. Including the observed kinematic misalignment in our intrinsic shape study shows that the fast rotators are predominantly axisymmetric, with only very little room for triaxiality. For the slow rotators though there are very strong indications that they are (mildly) triaxial.

Key words: galaxies: elliptical and lenticular, cD — galaxies: structure

1 INTRODUCTION

Shape is a very basic property of a galaxy, yet it contains strong constraints for its formation history, with different merger, accretion and assembly scenarios resulting in different shapes. Still, intrinsic shapes of individual galaxies are not readily obtained: detailed photometry and kinematical information is needed to construct a dynamical model of a galaxy, and constrain its shape (e.g. Statler 1994; Statler, Lambright & Bak 2001; van den Bosch & van de Ven 2009). Therefore, many studies to obtain intrinsic shapes of galaxies have focused on large samples, using statistical methods to obtain the underlying intrinsic shape *distribution* of a particular galaxy population (e.g., Hubble 1926; Sandage, Freeman & Stokes 1970; Lambas, Maddox & Loveday 1992; Tremblay & Merrit 1996; Ryden 2004; Vincent & Ryden 2005; Ryden 2006; Kimm & Yi 2007; Padilla & Strauss 2008; Méndez-Abreu et al. 2010; Yuma, Ohta & Yabe 2012). These studies rely on measurements of the observed ellipticities $\epsilon = 1 - b/a$, with b/a the observed axis ratio of the galaxy image, and, in principle, do not require kinematic information (although as we mention later inclusion of kinematic misalignment provides additional constraints on the shape distribution, e.g. Binney 1985; Franx, Illingworth & de Zeeuw 1991). Especially the Sloan Digital Sky Survey (SDSS) has been a major provider for imaging used in shape studies: recent results based on this survey include the non-circularity of discs in spiral galaxies (Ryden 2004; Padilla & Strauss 2008) and the presence of triaxial and prolate galaxies in the early-type galaxy population (Vincent & Ryden 2005; Kimm & Yi 2007).

The selection of the galaxy populations in these previous studies has been predominantly based on morphology, colour and structural parameters such as Sérsic index (Sérsic 1968). With the advent of integral-field spectroscopic studies we have an additional parameter to base our sample selection on: kinematic structure. In this paper we exploit this opportunity to make a stricter selection by using the ATLAS^{3D} sample: a volume-limited survey of 260 nearby early-type galaxies (Cappellari et al. 2011a, hereafter Paper I), that includes integral-field spectroscopy obtained by the SAURON spectrograph (Bacon et al. 2001). We are now able to make a distinction between two classes of early-type galaxies, fast and slow rotators, based on their extended kinematic properties, and as such obtain a cleaner galaxy population sample.

In Section 2 we describe the properties of the ATLAS^{3D} sample and the dataset that we use for the shape inversion in this paper, while in Section 3 we explain our methods and show our results for an axisymmetric shape inversion. Section 4 contains a discussion and interpretation of our results, and we further investigate the assumption of axisymmetry, by including kinematic misalignment angles in our shape analysis. We summarize our work in Section 5, and provide additional formularium for our shape distributions in the appendices.

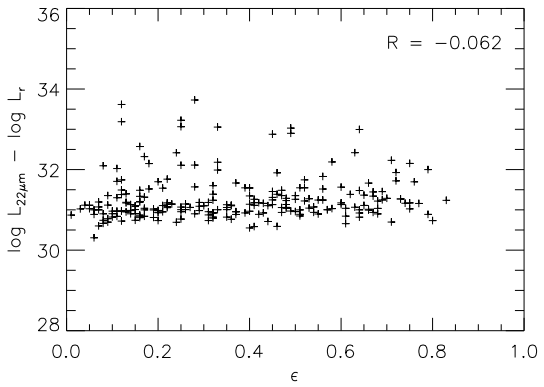

Figure 1. Ratio between mid-infrared and optical flux (expressed as a difference in magnitudes) as a function of ellipticity for 231 galaxies in our sample. There is no correlation between these two quantities, indicating that our sample is not contaminated with late-type galaxies of preferred orientations, see text for details. The linear Pearson correlation coefficient R is printed in the top right corner.

2 OBSERVATIONS

2.1 Sample

The ATLAS^{3D} sample was selected from a volume-limited parent sample of 871 galaxies in the nearby Universe. This parent sample consists of all galaxies within a distance of 42 Mpc, down to a total luminosity of -21.5 M_K, based on the 2MASS extended source catalog (Jarrett et al. 2000). The sample had to be observable with the William Herschel Telescope (WHT) from La Palma, Spain, so that only galaxies with sky declination $|\delta - 29°| < 35°$ were included. Finally, the dusty region near the Galaxy equatorial plane $|b| < 15°$was excluded, with b the galactic latitude. From this parent sample, early-type galaxies were morphologically selected based on visual inspection of multi-colour images from SDSS DR7 (Abazajian et al. 2009) or B-band DSS2-blue images[1], resulting in a sample of 260 galaxies. The main selection criteria here were the apparent lack of spiral arms in face-on, and dust lanes in edge-on systems, indicating that our selected galaxies are indeed early-types. For more details on the selection and properties of the ATLAS^{3D} sample, we refer the reader to Paper I. Important for our work here is to keep in mind that our sample is complete and has integral-field kinematics available for all galaxies (Paper I; Krajnović et al. 2011, hereafter paper II; Emsellem et al. 2011, hereafter Paper III), allowing us to perform a shape inversion on fast and slow rotators separately.

2.2 Investigation of selection bias

For a statistical shape analysis as described in this paper to work, we must have a galaxy sample that is randomly oriented on the sky, such that our assumption of random viewing angles is a valid one. Our selection criteria for removing late-type galaxies from our sample (i.e., presence of spiral arms and/or dust lanes) may however differ in reliability for different viewing angles and could in principle introduce a bias in our sample. For instance, if our method of detecting dust lanes in edge-on galaxies is not effective enough to identify all edge-on late-type galaxies present, then our sample would be contaminated with an extra population of flat spirals. We also note that although edge-on galaxies with large scale dust lanes were excluded from the ATLAS^{3D}sample, galaxies with small, central dust features were not, as these are not related to galaxy-wide spiral arms. To investigate whether a bias is present, we extract band W4 22μm from the archive of the Wide-field Infrared Survey Explorer (WISE; Wright et al. 2010) for 231 galaxies in our sample. These fluxes are presented in Davis et al. (2014) and are measured within elliptical apertures, see the on-line[2] WISE documentation for more details. If indeed our sample suffers from harbouring edge-on spiral galaxies, which are dustier than early-type galaxies, then we expect the ratio between the dust-tracing mid-infrared and the star-tracing optical fluxes to change as a function of ellipticity. Figure 1 shows that this is not the case: there is no correlation between mid-infrared to optical flux ratio and ellipticity for the galaxies in our sample. This is confirmed by the linear Pearson correlation coefficient R, which is small (-0.062). The mid-infrared fluxes correlate with the optical fluxes as expected (Temi et al. 2009, Davis et al. 2014), which is a necessary condition for our test to work. We therefore conclude that the ATLAS^{3D}sample of early-type galaxies is indeed randomly distributed on the sphere of viewing angles.

2.3 Observed shape and misalignment distribution

The ellipticities of the galaxies in our sample were measured and presented in Paper II, and we refer the reader there for details. Briefly, for 212 galaxies in our sample SDSS DR7 r-band imaging is available (Abazajian et al. 2009) and for 46 galaxies not covered by this survey we obtained comparable r-band imaging with the Wide Field Camera on the Isaac Newton Telescope (INT) on La Palma. These observations and their data reduction are presented in Scott et al. (2013, Paper XXI). For the two remaining galaxies we used 2MASS K-band observations instead.

Since we are interested in the global shapes of the galaxies, and to avoid our analysis being dominated by e.g. central bars, we measured the ellipticities using the moment of inertia of the surface brightness distribution on the sky subtracted images, with bright stars and neighbouring galaxies masked (see Paper II for a detailed description of this method). This way, all components in the galaxy contribute to a global ellipticity measurement, which would not be the case if we measured ellipticity only at a fixed radius. However, this method of measuring ellipticity does introduce a bias towards the shapes at larger radius. Only pixels above a certain threshold, 3 times the rms of the sky, were included in the measurements. For galaxies that were dominated by bars, we lowered the threshold to 0.5 or 1 times the sky rms,

[1] available on-line at http://archive.eso.org/dss

[2] http://wise2.ipac.caltech.edu/docs/release/allsky/

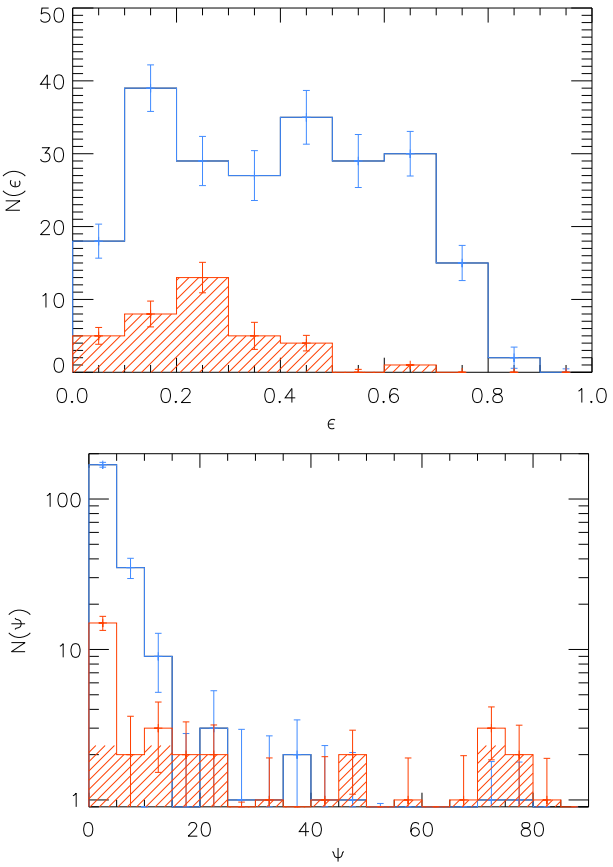

Figure 2. Top: histogram of observed ellipticities. The distribution of fast rotators is presented in blue (open histogram), while the slow rotators are denoted by the red, dashed histogram. The 1-σ errorbars are based on Monte Carlo simulations, taking the individual measurement errors for each galaxy into account. Bottom: same as top panel, but now for observed kinematic misalignments. The y-axis is now given in log-scale.

to better probe the underlying stellar disc. This resulted in ellipticity measurements representative of the galaxy out to typically 2.5 to 3 effective radii. We compared these global ellipticity values to radial profiles, determined by fitting ellipses along isophotes with KINEMETRY (Krajnović et al. 2006), and found that these values agree well: the standard deviation of the differences between the two measurements was 0.03, see Paper II.

Uncertainties were determined by repeating the ellipticity measurements for each galaxy at different thresholds (0.5, 1, 3 and 6 times the sky rms) and the standard deviations of these measurements were adopted as errors. We show the resulting observed ellipticity distribution for our sample in Figure 2, both for the fast and slow rotators. The 1-σ errors in the histograms have been determined using Monte Carlo simulations, based on the errors in ellipticity of the individual galaxies. These individual values can be found in Table 1 of Paper II.

Paper II also provides values for the photometric and kinematic position angles, used to measure the kinematic misalignment Ψ between the projected rotation axis and the minor axis of a galaxy. The photometric position angle was measured on the SDSS, INT or 2MASS imaging, using the same method as described above for the ellipticity. The kinematic position angle was measured on the SAURON velocity maps using the method outlined in Appendix C of Krajnović et al. (2006). Both these position angles, as well as the kinematic misalignment are tabulated in Table 1 of Paper II, and we show the histogram of observed kinematic misalignments for fast and slow rotators in Figure 2. The majority of the fast rotators have small kinematic misalignments, with 76 per cent having misalignments smaller than 5°. The slow rotators on the other hand show more kinematic misalignment, with less than half of them (44 per cent) having $\Psi < 5°$.

3 INTRINSIC SHAPE DISTRIBUTIONS FOR FAST AND SLOW ROTATORS

Fast and slow rotators are two distinct classes of early-type galaxies, as was shown by Emsellem et al. (2007) and Cappellari et al. (2007). They defined slow rotators to have a specific angular momentum $\lambda_R < 0.1$, while fast rotators in their classification have $\lambda_R > 0.1$. Later, this classification was refined in Paper III, considering the regularity of the velocity maps (Paper II). In the resulting classification, the separation between slow and fast rotators takes the projected ellipticity of the systems into account, with slow rotators having $\lambda_R < 0.31\sqrt{\epsilon}$, and fast rotators $\lambda_R > 0.31\sqrt{\epsilon}$. Figure 6 in Paper III illustrates that this new division of the early-type galaxy population into fast and slow rotators nicely follows the kinematic classification based on the velocity maps. This figure also shows that λ_R is a more reliable separator between fast and slow rotators than the V/σ_e quantity, with V the velocity amplitude, and σ_e the velocity dispersion measured within one R_e. We refer to paper III for more details on this classification scheme. Important for our analysis is that the separation of our sample in slow and fast rotators does not introduce any biases in viewing directions: this is discussed in Paper III (see their sections 5.1 and 5.2), but also shown in simulations performed independently by Jesseit et al. (2009) and Bois et al. (2011, Paper VI). In particular, Jesseit et al. (2009) perform an extensive study of variations in λ_R with inclination, and find that λ_R does not deviate significantly from its maximum value for a large range of viewing angles. This makes λ_R a reliable and robust estimator of the intrinsic angular momentum. Jesseit et al. (2009) quote a confusion probabiliy of 4.6 per cent of mistakingly classifying a fast rotating galaxy as a slow rotator. They add that this probability will be even lower in practise, as their simulated merger sample has a significantly larger number of prolate shaped galaxies than observed in galaxy surveys, and most of the wrongly classified galaxies in their sample fall into this category. In our ATLAS^{3D}sample we only have two clear examples of prolate galaxies: one of them is classified as a fast rotator, but both have non-regular rotation (Paper II). We therefore are confident that any contaminations in our sample due to misclassification of fast and slow rotators is negligible for our intended purposes.

Based on papers II and III fast rotators are galaxies with regular, aligned velocity fields that often possess discs and bars, while slow rotators are often kinematically misaligned, have kinematically distinct cores (KDCs) and are located on

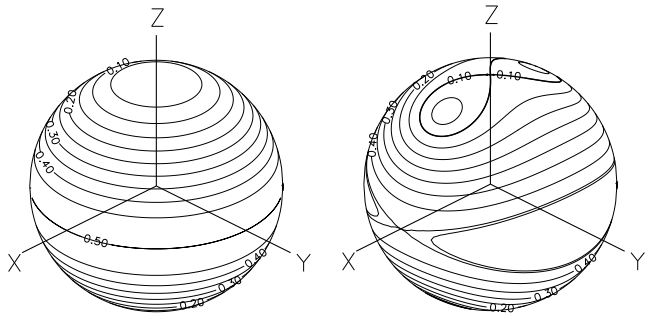

Figure 3. Contours of constant ellipticity on the sphere of viewing angles, for an oblate galaxy ($p = 1$ and $q = 0.5$, left) and a triaxial galaxy ($p = 0.9$ and $q = 0.5$, right). The ellipticity varies between 0 and $1 - q$.

the more massive end of the luminosity function. In addition, Cappellari et al. (2011b, hereafter Paper VII) show that slow rotators are predominantly found in the high-density environment, which for our sample is the core of the Virgo cluster, and are almost non-existent in the field.

These all are hints that fast and slow rotators have different formation scenarios (see also Paper VI). It is therefore unlikely that these two classes of objects have a similar shape distribution, and indeed a simple Kolmogorov-Smirnov test confirms at the 5 per cent significance level that the ellipticity distributions of the fast and slow rotators in our sample are not drawn from the same underlying distribution ($p_{\rm KS} = 3\times10^{-5}$, see also Figure 2). A Mann-Whitney U-test also rejects the notion that the two ellipticity distributions have the same mean ($p_{\rm MW} = 1.7\times10^{-4}$). We therefore consider the fast and slow rotators separately, when inverting their shape distributions. As explained below, we assume an axisymmetric underlying shape distribution in this section, and we will explore deviations from this axisymmetric assumption later on in this paper in § 4.4.

3.1 Intrinsic and observed shape distributions

The intrinsic shape of a galaxy can be modeled as an ellipsoid, with intrinsic axis ratios p and q, such that $1 \geqslant p \geqslant q \geqslant 0$. The observed shape or ellipticity ϵ of a galaxy then depends on its intrinsic shape and on the viewing angles (inclination ϑ and azimuthal angle φ), such that $\epsilon = \epsilon(p, q, \vartheta, \varphi)$, see Figure 3 for an example of ellipticity plotted on the sphere of viewing angles. It is therefore impossible to deduce the intrinsic shape (p, q) for an individual galaxy, based on its observed ellipticity only. Early work (e.g. Hubble 1926; Sandage et al. 1970) therefore used the observed distribution $F(\epsilon)$ for a sample of galaxies, assuming that the galaxies were axisymmetric ($p = 1$ for oblate galaxies, $p = q$ for prolate galaxies) to determine the intrinsic shape distribution $f(q)$. This distribution is then uniquely determined, assuming that the galaxies are oriented randomly in space (random viewing angles).

For triaxial galaxies ($p \neq 1$) this is no longer the case, as $F(\epsilon)$ cannot uniquely determine $f(p, q)$ (e.g. Binggeli 1980; Binney & de Vaucouleurs 1981). Binney (1985) and subsequently Franx et al. (1991) showed that progress could be made by use of the kinematic information of the galaxies, namely by incorporating the kinematics misalignment angle (Ψ) between the observed minor axis and the projected rotation axis in the probability distribution[3]. $F(\Psi, \epsilon)$ is however also not able to uniquely define $f(p, q)$, as Ψ also depends on the intrinsic rotation axis, which for a triaxial galaxy can lie anywhere in the plane containing the short and long axis of the galaxy (see for example Franx et al. 1991). In an oblate galaxy, however, the rotation axis coincides with the short axis of the system, and no kinematic misalignment will be observed.

Our integral-field observations show that the fast rotators in our sample have zero or at most very small misalignments, and for this reason we first assume that the fast rotators are exactly oblate. This assumption allows us to invert the observed ellipticity distribution $F(\epsilon)$ to obtain the distribution of intrinsic flattening $f(q)$ of the fast rotators. For this inversion we use Lucy's method (1974), which is an iterative technique to solve for the underlying distribution function. We relax this assumption of oblateness in § 4.4, where we put an upper limit on the deviations from perfectly oblate shapes, using the observed kinematic misalignments as an extra constraint. Note that in the studies mentioned above, and in the analysis we present in this paper, galaxies are approximated by triaxial spheroids, while in reality many of them consist of separate bulge and disc components. By measuring our ellipticities at large radius, we assume that for disc-dominated galaxies we can ignore any bulge (and bar) contributions, and that we are mostly probing the outer disc, while for bulge-dominated galaxies we will be mostly sensitive to the shape of the spheroid.

3.2 The intrinsic shapes of fast rotators

We first consider our fast rotators to be oblate systems, as validated by their small kinematic misalignment. For oblate galaxies, observed ellipticity is a function of intrinsic flattening q and inclination ϑ only:

$$e = (1 - \epsilon)^2 = \cos^2\vartheta + q^2 \sin^2\vartheta, \quad (1)$$

with e the eccentricity, introduced here to simplify some of our notations. Assuming random orientations, integrating ϑ over the sphere of viewing angles then yields a probability function $P(\epsilon|q)$ such that:

$$P(\epsilon|q) = \frac{\sqrt{e}}{\sqrt{1-q^2}\sqrt{e-q^2}}. \quad (2)$$

With Lucy's method (1974) we solve for the intrinsic shape distribution $f(q)$:

$$F(\epsilon) = \int f(q) P(\epsilon|q) dq. \quad (3)$$

For the observed distribution $F(\epsilon)$ we approximate each fast rotator galaxy with a Gaussian distribution function, centred at its measured ellipticity, with a standard deviation given by its measurement error. $F(\epsilon)$ is then the superposition of these 224 Gaussian functions (one for each fast rotator), see top panel of Figure 4. We applied some mild smoothing with a boxcar before inverting this curve. We

[3] We present a shape analysis based on kinematic misalignment in Appendix B.

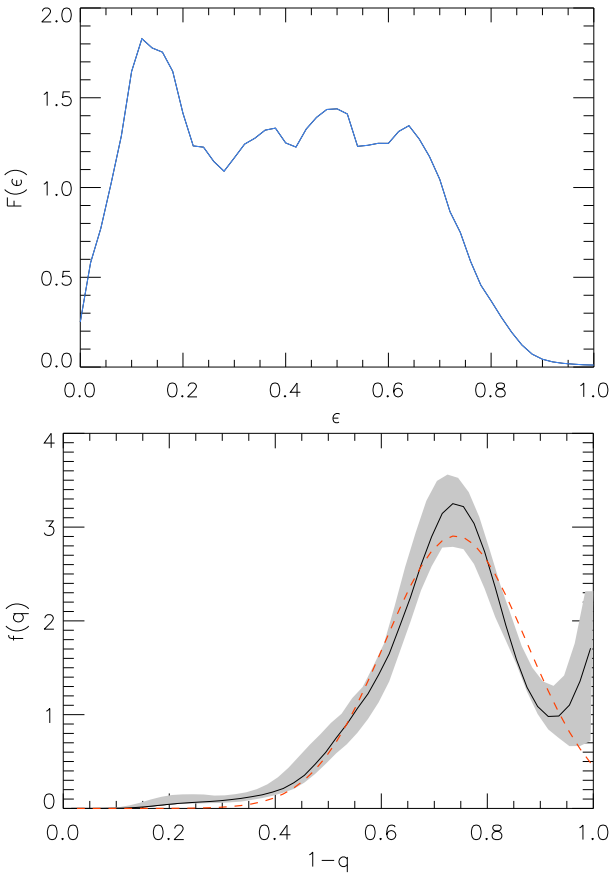

Figure 4. Top panel: observed distribution $F(\epsilon)$ for the 224 fast rotators in the ATLAS^{3D}sample, obtained by approximating each galaxy as a Gaussian function with mean given by its measured ellipticity, and width (standard-deviation) by its 1-σ measurement error. Some mild smoothing is applied. Lower panel: the inverted intrinsic shape distribution $f(q)$ for the fast rotators, shown by the black solid line. We plot $1-q$ on the horizontal axis such that round objects are on the left and flattened ones on the right, to be consistent with our observed ellipticity plots. The red solid line shows a Gaussian fit to the intrinsic shape distribution. The intrinsic shape distribution peaks around $q = 0.25$, but has an extended tail towards rounder shapes. The grey area shows the area enclosing 95 per cent of inversions for our Monte Carlo simulations (see text for details).

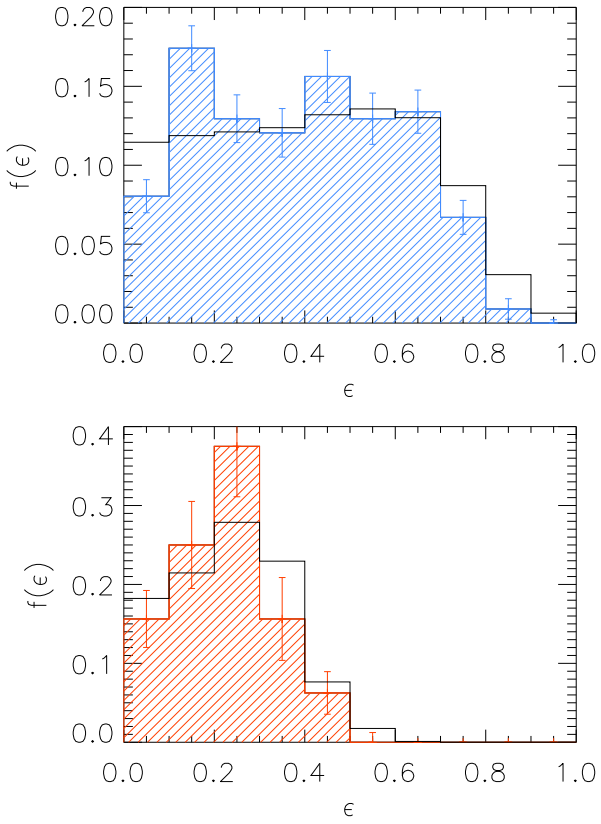

Figure 5. Top panel: observed ellipticity distribution of the fast rotators in the ATLAS^{3D}sample (blue dashed histogram), compared to a mock ellipticity distribution of 10^6 galaxies (black open histogram), drawn from the intrinsic shape distribution $f(q)$ with random viewing angles. Bottom panel: same as above, but now for the slow rotators (red dashed histogram).

checked that Lucy's method converges within 25 iterations, and the resulting inverted distribution $f(q)$ is shown in the lower panel of Figure 4, as the black solid line. The intrinsic flattening distribution $f(q)$ can be approximated by a Gaussian function (red solid line), with mean $\mu_q = 0.26$ and standard-deviation $\sigma_q = 0.13$. Interestingly, this mean value is very similar to the intrinsic flattenings found in similar studies for spiral galaxies (e.g. Lambas et al. 1992; Ryden 2006; Padilla & Strauss 2008), and we will discuss this in more detail in § 4.1.

Although our inversion does technically take the measurement errors of our observed ellipticities into account by approximating each measurement as a Gaussian, we should ask ourselves how sensitive our inversion is to small deviations in the so obtained observed distribution $F(q)$. We therefore repeated our inversion another 100 times with a Monte Carlo simulation: we again approximated our observed ellipticities with a Gaussian function and applied some mild smoothing, but for its mean we drew from a Gaussian distribution, centred on the observed ellipticity and with a standard deviation given by the measurement error. We show the central 95 per cent of the resulting inversion curves $f(q)$ in Figure 4 with the grey shaded area. This figure shows that our inversion is fairly robust: we fitted Gaussians to all of $f(q)$ resulting from this Monte Carlo exercise, and found that the best fitting Gaussian of the overall intrinsic shape distribution parametrized with mean $\mu_q = 0.25 \pm 0.01$ and $\sigma_q = 0.14 \pm 0.02$.

In the top panel of Figure 5 we compare the predicted ellipticity distribution from our model with our observations, by generating a mock sample of 10^6 galaxies, drawn from the intrinsic shape distribution $f(q)$. The predicted ellipticity distribution does deviate somewhat from our observed distribution, but a one-sided KS-test shows that these deviations are not significant ($p_{\rm KS} = 0.19$) given the relatively small sample size of our observed sample.

We also investigated whether we could find differences in intrinsic shape distributions based on environment. Since different formation processes are at play in clusters than in the field (see e.g. Blanton & Moustakas 2009 for a review), we could expect that therefore the intrinsic shape distribution of fast rotators in the Virgo cluster would be different

from that for fast rotators in less dense environments. We did however not detect any significant deviations in shape distribution between these two sets of galaxies, as could indeed already have been inferred from a Kolmogorov-Smirnov test on the observed ellipticity distributions. The hypothesis that the ellipticity distributions of both field and Virgo fast rotators are drawn from different underlying distributions is rejected at the 5 per cent significance level with $p_{\rm KS} = 0.96$, while also the Mann-Whitney U-test rejects the hypothesis of different means for the distributions with $p_{\rm MW} = 0.46$, at the same significance level (see left panel of Figure 6). Similarly, we also did not find any differences in shape distributions and means of distributions if we divide our sample based on mass[4] ($M_{\rm JAM} < 10^{11} M_{\odot}$ versus $M_{\rm JAM} > 10^{11} M_{\odot}$), with $p_{\rm KS} = 0.79$ and $p_{\rm MW} = 0.29$ (right panel Figure 6). These masses were determined based on dynamical modeling, and the values for individual galaxies are listed in Cappellari et al. (2013a, paper XV).

3.3 The intrinsic shapes of slow rotators

The slow rotators in our sample show clear signs of triaxiality, such as kinematic misalignment. For the moment however we approximate these systems as oblate, so that we can invert their observed ellipticity distribution to obtain an estimate of their intrinsic flattening.

Following the same technique as described for the fast rotators, we then arrive at the intrinsic shape distribution shown in the bottom-left panel of Figure 7. The distribution is clearly double peaked, with the larger peak being well approximated with a Gaussian centred at $\mu_q = 0.61$ with $\sigma_q = 0.09$. The smaller peak around $q = 0.3$ coincides with the shape distribution of the fast rotators. It therefore looks like our sample of slow rotators consists of two populations, with the majority being roundish objects, supplemented with a second smaller population of more flattened galaxies. Indeed, 4 of our 36 slow rotators are flattened, counter-rotating disk galaxies (so-called 2σ-galaxies exhibiting a double peaked profile in velocity dispersion, see Paper II for details). These are NGC3796, NGC4191, NGC4528 and NGC4550 with the latter the most extreme case with $\epsilon = 0.68$. Removing these galaxies from our slow rotator sample did not change the larger peak significantly (the best-fit Gaussian remained the same), but did remove the secondary peak. In fact, removing just NGC4550 from the slow rotator sample resulted in the disappearance of the secondary peak altogether, showing the sensitivity of our inversion method. Though the parameters of the best-fit Gaussian remain the same when removing the 2σ-galaxies, most of the inverted distributions $f(q)$ from the Monte Carlo simulations that define the grey 95 per cent area in the lower right panel of Figure 7 are shifted towards rounder shapes: the Gaussians fit to these Monte-Carlo inversions are $\mu_q = 0.63 \pm 0.01$ and $\sigma_q = 0.09 \pm 0.01$.

As for the fast rotators, we compare the ellipticity distribution of a mock galaxy sample drawn from the intrinsic distribution $f(q)$ derived above, to the observed ellipticities in the ATLAS$^{\rm 3D}$sample. The results are shown in the bottom panel of Figure 5. A one-sided KS-test indicates that we can indeed accept the hypothesis that the observed distribution ($p_{\rm KS} = 0.29$) was drawn from the proposed intrinsic distribution.

In Figure 8 we contrast the intrinsic flattening of fast rotators and slow rotators in our ATLAS$^{\rm 3D}$ sample. It is obvious that on average the fast rotators are much more flattened than the slow rotators, as already emphasized in our morphological classification 'comb' diagram in Figure 2 of Paper VII, though it is interesting to see that there is also a large overlap between the two distributions, with the tail towards rounder shapes of the fast rotator distribution overlapping with the one of the slow rotators.

4 DISCUSSION

4.1 Fast rotators and spirals

Our fast rotators are significantly flatter than the slow rotators in our sample, and are in fact close to the intrinsic flatness observed in spiral galaxy populations, although we do observe a tail towards rounder shapes. Lambas et al. (1992) for instance find $\mu_q = 0.25$ for their sample of 13,482 spiral galaxies, based on imaging of the APM Bright Galaxy Survey, which is consistent with the intrinsic flattening that we found in § 3.2 for the fast rotators. In contrast, the 2135 elliptical and 4782 lenticular galaxies in their sample are best described with intrinsic flattening $\mu_q = 0.55$ and $\mu_q = 0.59$, respectively. They note that all three galaxy populations need to be slightly triaxial, which is something we will explore in § 4.4. More recently, Padilla & Strauss (2008) reported similar results based on SDSS Data Release 6 imaging, with their 282,203 spirals having $\mu_q = 0.21 \pm 0.02$, although their 303,390 ellipticals are flatter than the Lambas et al. result, with $\mu_q = 0.43 \pm 0.06$. We note that the slow rotators in our sample with $\mu_q = 0.63$ are slightly rounder than the elliptical samples in both these previous studies. These deviations could be caused by our smaller sample sizes, but could also be indicative of the fact that we classified our early-type galaxies kinematically, while the early-type galaxies samples based on imaging only contain a mixture of fast and slow rotators. Indeed, in Paper III we show that 66 per cent of the galaxies in the ATLAS$^{\rm 3D}$ sample classified as elliptical (E) are in fact fast rotators. Another recent study of axis ratio measurements at both local and higher redshift ($1 < z < 2.5$) finds that the total population of early-type galaxies in both samples is well-described with an intrinsic shape distribution consisting of a triaxial, round component, and an oblate, flattened ($q \sim 0.3$) component, with the fractions of these two populations varying as a function of stellar mass and redshift (Chang et al. 2013). These results would agree with our observations of the different shape distributions for our slow and fast rotator sample.

That the fast rotators have a similar shape distribution to spiral galaxies is in line with previous studies that have

[4] Mass was taken from Paper XV as $M_{\rm JAM} = L \times (M/L)_e \approx 2 \times M_{1/2}$, with $(M/L)_e$ the total mass-to-light ratio measured within one half-light radius R_e, with self-consistent Jeans Anisotropic modelling, and $M_{1/2}$ the total mass within a sphere of radius R_e, enclosing half of the galaxy light. The contribution of dark matter to $(M/L)_e$ within one R_e is small (see Paper XV for details), so $M_{\rm JAM}$ can be interpretated as a dynamical estimate of stellar mass. Throughout this paper, we will therefore refer to $M_{\rm JAM}$ as a stellar mass estimate.

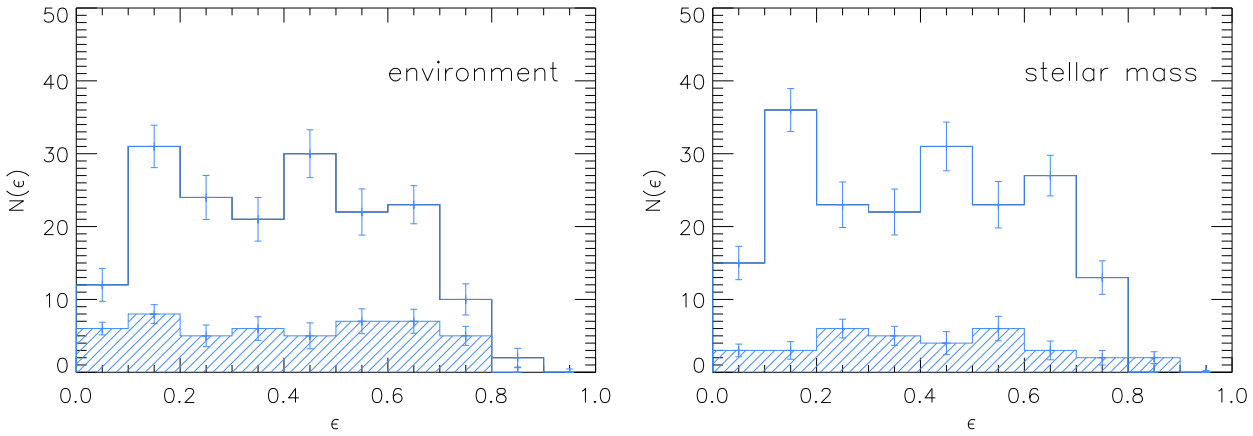

Figure 6. Histogram of observed ellipticities for fast rotators, divided based on environment (left) and mass $M_{\rm JAM}$ (right). The left plot shows the 49 fast rotators in Virgo (dashed histogram) versus the 175 field fast rotators (open histogram) for our sample. The right plot shows the fast rotators with $M_{\rm JAM} > 10^{11} M_{\odot}$ (34 galaxies, dashed histogram) versus the lower mass fast rotators with $M_{\rm JAM} < 10^{11} M_{\odot}$ (190 galaxies, open histogram). The 1-σ errorbars are based on Monte Carlo simulations, taking the individual measurement errors for each galaxy into account. The division in environment and in stellar mass do not result in statistically significant different shape distributions. See text for details.

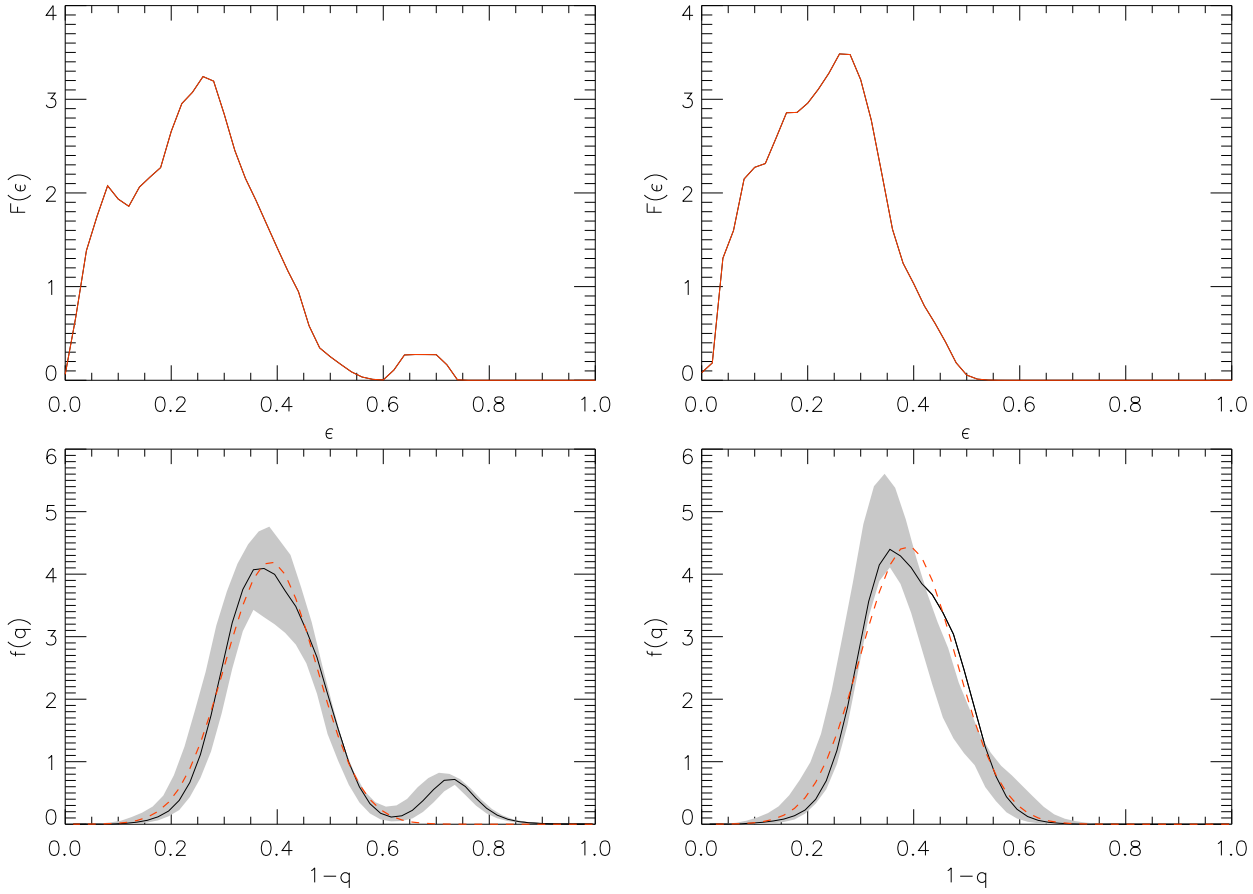

Figure 7. Top left panel: observed distribution $F(\epsilon)$ for the 36 slow rotators, similar to top panel of Figure 4. Bottom left panel: inverted shape distribution $f(q)$ for the 36 slow rotators in our sample (solid black line). The red dashed line shows a Gaussian fit to the distribution, and the grey area indicates a 95 per cent spread around our Monte-Carlo simulations (see text for more detail). Right panels: same as left panels, but now the four 2σ-galaxies with counter-rotating discs have been removed from the slow rotator sample, resulting in a cleaner and overall slightly rounder shape distribution. We use this instrinsic distribution for our subsequent discussions and analysis.

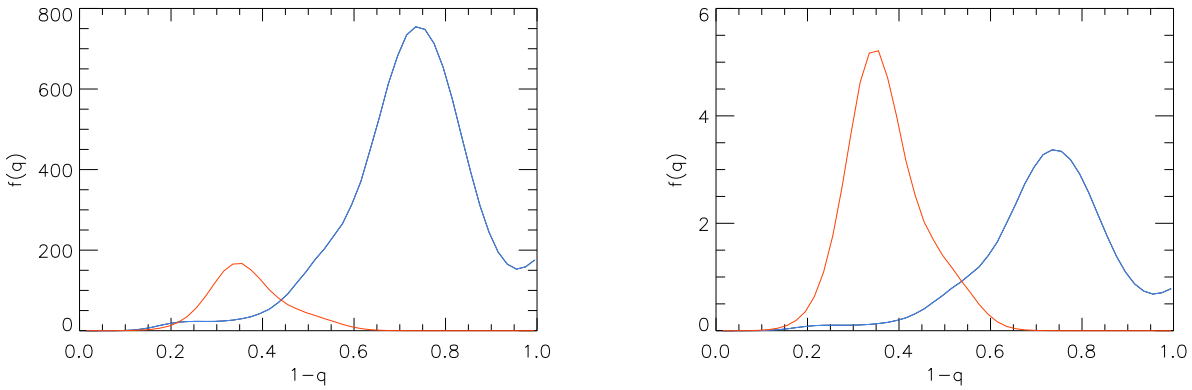

Figure 8. Comparing the oblate intrinsic shape distributions $f(q)$ of fast (blue solid line) and slow rotators (red solid line). Left: distribution scaled with absolute number of galaxies in each sample (224 fast rotators versus 32 slow rotators). Right: normalized distributions.

shown that spiral galaxies display a large range of disc-to-total (D/T) ratios (e.g. Graham 2001; Weinzirl et al. 2009), which is also found to hold true for the galaxies in our sample: Krajnović et al. (2013, paper XVII) performed bulge-disc decompositions for the ATLAS^{3D} sample and found that 83 per cent of the non-barred galaxies in the sample have disc-like components. The resemblance between spiral and early-type galaxies was most notably pointed out by Van den Bergh (1976), who redesigned the Hubble tuning fork to include a parallel sequence of lenticular galaxies (S0) to the spiral galaxies, with decreasing D/T ratios when moving from S0c to S0a closer to the elliptical galaxies.

In Paper VII we revisited Van den Bergh's classification scheme by showing that it are the fast rotators who form a parallel sequence to the spiral galaxies, re-emphasizing the importance of this parallelism to understand how galaxies form, see also Laurikainen et al. (2011) and Kormendy & Bender (2012).

4.2 Shape as a function of stellar mass

In § 3.2 we showed that there is no clear difference between shape distributions of fast rotators above and below a stellar mass of $10^{11}\,M_\odot$ (see Figure 6, right-hand plot). At first sight, this seems in contradiction with Tremblay & Merritt (1996), and more recently, with van der Wel et al. (2009) and Holden et al. (2012), who based on a sample of quiescent galaxies selected from the Sloan Digital Sky Survey, find that galaxies with stellar mass $M_* > 10^{11}\,M_\odot$ are predominantly round, while galaxies with lower masses have a large range in ellipticity. This change in shape at a characteristic mass of $M_{\rm JAM} \sim 2 \times 10^{11}\,M_\odot$ is also evident in our sample when studying the mass-size relation (Figure 7 of Cappellari et al. 2013b, hereafter Paper XX). However, as already illustrated in Figure 14 of Paper XX, the picture changes when we include the kinematical information. In Figure 9 we show the ellipticities of both fast and slow rotators as a function of stellar mass, and we also indicate different kinematical classes as defined in Paper II: class *a* includes galaxies which do not show any significant rotation (non-rotators), class *b* comprises galaxies with complex velocity maps, but without any distinct features, class *c* consists of galaxies with kinematically distinct cores (including counter-rotating cores), class *d* has galaxies with double peaks in their dispersion maps (the 2σ-galaxies, consisting of counter-rotating discs) and finally, class *e* is the group of galaxies with regularly rotating velocity maps. Taking this subdivision into account, we note that above $M_{\rm JAM} \sim 10^{11}\,M_\odot$ the number of fast rotators quickly declines, and the highest mass galaxies are predominantly round non-rotators (class *a*). This indicates that the observed trend with more massive galaxies being on average rounder than less massive ones can be explained by the increasing fraction of slow rotators at high masses, and that the orbital make-up drives the dependency of shape on mass.

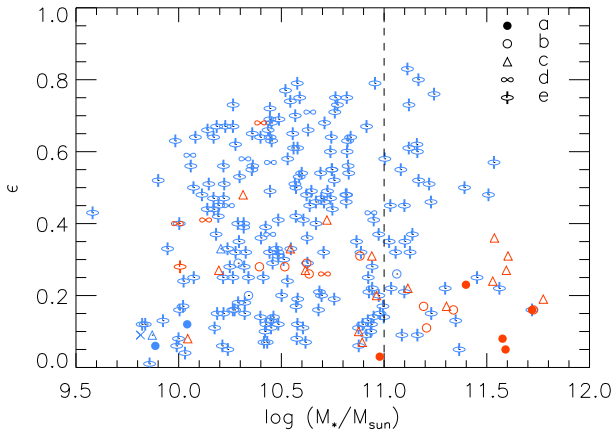

Figure 9. Ellipticity as a function of stellar mass (as introduced in § 3.2), for fast (blue symbols) and slow rotators (red symbols). Fast rotators show a large spread in ellipticity over all mass ranges, while the most massive galaxies are predominantly round slow rotators. The symbols labeled *a*-*e* define different kinematical classes, and are explained in the text. The galaxy marked with a cross (X) could not be kinematically classified.

Figure 10 shows the fraction of galaxies with axis ratios below 0.8, 0.6 and 0.4 as a function of stellar mass for the total ATLAS^{3D}galaxy sample, and compares these fractions with the results from van der Wel et al. (2009). The ATLAS^{3D} fractions remain constant up to $M_* \sim 10^{11.3}$, as our sample is dominated by fast rotators (216/240 galax-

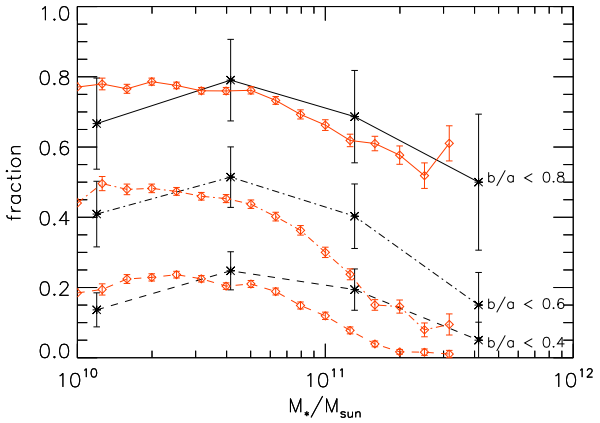

Figure 10. Fraction of galaxies with axis ratio smaller than 0.8 (solid line), 0.6 (dotted-dashed line) and 0.4 (dashed line), for the ATLAS^{3D}sample (black stars) and van der Wel sample (red diamonds), as a function of stellar mass M_*. For the ATLAS^{3D}sample, the bins boundaries (in $\log M_\odot$) are given by 10.3, 10.8 and 11.3. The van der Wel sample shows a clear trend with more massive galaxies being rounder: this trend is also seen in the ATLAS^{3D}sample in the largest mass bin, which contains a relatively large fraction of slow rotators.

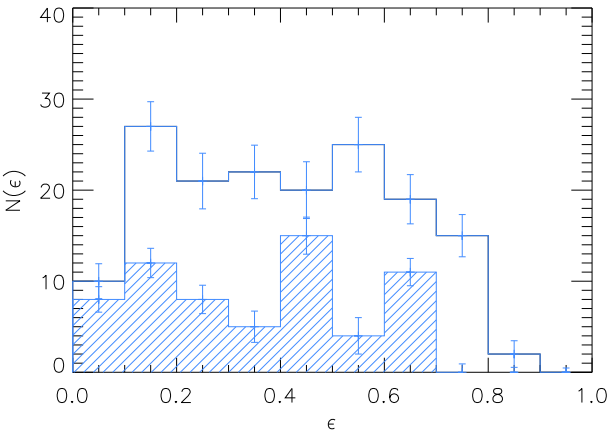

Figure 11. Observed ellipticity histogram for the barred (dashed histogram) and non-barred (open histogram) fast rotators. The non-barred galaxies in our sample are intrinsically flatter than the barred galaxies, but this is a selection effect, as bars are easier detected in face-on than edge-on galaxies, see text for details.

ies) in that mass range. The fractions from the van der Wel sample show a clear trend between axis ratio and stellar mass, with more massive galaxies being rounder. We reproduce that trend in our sample in the highest massbin ($M_* > 10^{11.3}$), which contains a relatively large number of slow rotators (12/20 galaxies).

4.3 A lack of round galaxies?

For a family of perfect oblate objects, we expect the shape distribution to peak at $\epsilon = 0$ (see Equation 2, which behaves asymptotically at $q = 1$). However, our observed ellipticity distribution for fast rotators decreases towards round shapes (see Figure 2). This lack of round galaxies has been observed before (e.g. Fasano & Vio 1991; Ryden 1996), and before investigating deviations from axisymmetry (§ 4.4), we first explore whether our selection or ellipticity measurement methods could be responsible for this observation.

Our measurements of ellipticity are based on moment of inertia, and a positive bias is introduced for nearly round objects, as negative ellipticities are not allowed. Tests conducted in Paper II show however that this positive bias is of order 0.02, and therefore too small to expel a significant number of galaxies out of the roundest ellipticity bin. The influence of bars on our ellipticity measurements would be of larger concern: although we obtain a global measurement of the ellipticity by using moment of inertia as opposed to a radius-dependent measurement, large bars could still significantly increase the ellipticity of their round host galaxies. To investigate this effect, we simulated perfectly oblate galaxies both with and without bars, following the methods outlined in Lablanche et al. (2012, paper XII), and observed these galaxies face-on (so at $\epsilon = 0$). We found that bars indeed increased the observed ellipticity to about 0.15, which is sufficient to move round galaxies from the roundest ellipticity bin into the next one. However, when splitting our sample of fast rotators into barred and non-barred galaxies (following the classification of Paper II), we find that the barred galaxies are on average rounder than the non-barred galaxies, contrary to what we expected based on our simulations (see Figure 11). This is however a selection effect: bars are more easily identified in face-on (round) galaxies than in edge-on (flattened) ones. It is therefore likely that there are still some undetected bars present in our galaxy sample at higher ellipticities, but this would not explain the possible deficiency of low ellipticity galaxies. We therefore conclude that it is very unlikely that barred galaxies are biasing our observed shape distribution towards flatter systems. The perceived lack of round galaxies is therefore either real, or has some other, more subtle cause. Despite this discrepancy however, we show in the next section by including the observed kinematic misalignment in our intrinsic shape analysis, that an oblate distribution is indeed a very good description of our fast rotator sample.

4.4 Deviations from axisymmetry

So far we have assumed that the fast rotators in our sample are oblate ($p = 1$) systems, motivated by the observation that almost all fast rotators have small or negligible misalignment. We now investigate whether a triaxial ($p \neq 1$) distribution would be preferred above an oblate one, using the observed kinematic misalignment Ψ as an additional constraint (Binney 1985; Franx et al. 1991).

We cannot use a Lucy inversion as above to invert the observed distribution, as we now have two observables (Ψ, ϵ) and three unknowns (p, q and the intrinsic misalignment $\theta_{\rm int}$, which is defined such that $\theta_{\rm int}$=0 corresponds to alignment of the intrinsic rotation axis with the short axis of the galaxy). We therefore fit the observed two-dimensional distribution $F(\Psi, \epsilon)$ to simulated distributions, generated by assuming a Gaussian distribution in q with mean and standard deviation μ_q and σ_q, and a log-normal distribution in $Y = \ln(1-p)$ with mean and standard deviation μ_Y and σ_Y, following e.g. Padilla & Strauss (2008). For $\theta_{\rm int}$ we assume that this angle only depends on the intrinsic shape, such

that $\theta_{\rm int}$ coincides with the viewing direction that generates a round observed ellipticity ($\epsilon = 0$, see right-hand plot of Figure 3). Mathematically, this corresponds to:

$$\tan\theta_{\rm int} = \sqrt{\frac{T}{1-T}}, \tag{4}$$

with T the triaxiality parameter defined by Franx et al. (1991) as:

$$T = \frac{1-p^2}{1-q^2}. \tag{5}$$

This assumption ensures that in systems close to oblateness, $\theta_{\rm int}$ is small and close to the short axis, and only increases for larger triaxiality. This assumption is valid for many self-consistent models (e.g., Hunter & de Zeeuw 1992; Arnold, de Zeeuw & Hunter 1994), and we will give a more detailed overview of the geometry and probability distributions for such systems in appendix A.

To determine the best-fitting simulated distribution, we calculate χ^2 as:

$$\chi^2(\mu_Y, \sigma_Y, \mu_q, \sigma_q) = \sum_{i,j} \frac{(O_{i,j} - M_{i,j})^2}{\delta O_{i,j}^2}, \tag{6}$$

where $O_{i,j}$ is the number of observed galaxies in each bin (Ψ_i, ϵ_j), with Ψ ranging from 0° to 90° and ϵ from 0 to 1, in binsteps of 5° and 0.1, respectively. The corresponding errors $\delta O_{i,j}$ are determined with Monte Carlo simulations, similar to the errors for the one-dimensional histograms in ϵ used before. For many of our bins with large misalignment this error is zero, which raises problems in our χ^2 determination. We therefore replaced these zero errors with artificially small values, corresponding to 0.1 times the minimal error in the total histogram. As a result, our χ^2 values are not statistically valid, but as we are interested in locating the best-fitting intrinsic distribution, we simply restrict our analysis to finding the minimal χ^2.

$M_{i,j}$ is the number of galaxies predicted for each bin given by the model, generated with the parameters $\mu_Y, \sigma_Y, \mu_q, \sigma_q$, and under the assumption that $\theta_{\rm int}$ is given by Equation 4. For each combination of these four parameters, we generate 100,000 random viewing angles and construct a distribution of an equal number of observed galaxies, drawing their intrinsic axis ratios p and q from their log-normal and Gaussian distributions, respectively. We then calculate for each galaxy its observed ellipticity and misalignment, using the formularium outlined in appendix A.

Before exploring the full grid of $\mu_Y, \sigma_Y, \mu_q, \sigma_q$, we first apply the above analysis to an oblate model, and only fit the one-dimensional histogram in ellipticity presented in Figure 2, ignoring the kinematic misalignment for the moment. As such, we are repeating the analysis presented in the previous section, though with a very different method. We plot the resulting χ^2 contours in Figure 12, both for our fast and slow rotator samples. For the fast rotators, we find a minimal χ^2 for $\mu_q = 0.33$ and $\sigma_q = 0.11$, which is somewhat rounder than the distribution we found with the direct inversion described in § 3.2, although the Gaussian fit to the intrinsic distribution does not take the tail towards higher q into account. For the slow rotators, we find $\mu_q = 0.66$ and $\sigma_q = 0.08$, which is very similar to the direct inversion described in § 3.3. This shows that the results we presented for the intrinsic shape distributions are not method dependent.

We now relax our assumption of oblateness on the fast rotator sample and explore the full grid $\mu_Y, \sigma_Y, \mu_q, \sigma_q$, and fit the two-dimensional histogram in Ψ and ϵ, with $\theta_{\rm int}$ given by Equation 4, as described above. The best-fit in this triaxial model space has values for μ_q and σ_q that are very close to the best-fit values for the oblate model discussed above, and therefore to limit the parameter search, we run a finer grid in μ_Y and σ_Y, keeping μ_q and σ_q fixed to 0.33 and 0.11, respectively. The best-fit model that we so obtain is very close to oblate, with $\mu_Y = -5.0$ (which corresponds to $p \sim 0.99$), and $\sigma_Y = 0.08$. In fact, $\mu_Y = -5.0$ is one of the boundaries in our grid, meaning that the best-fit model is as oblate as allowed by our grid choice. The resulting χ^2 contours are shown in Figure 13. Unfortunately, we cannot put any statistical significance to these contours, but we do note that models close to oblate (large negative μ_Y) are strongly preferred, while σ_Y is largely unconstrained.

Interestingly, the deviation from axisymmetry of our fast rotators is smaller than that of the spiral galaxies studied by Ryden (2006), who used the same methods to obtain a triaxial intrinsic shape distributions of her sample. She finds for her early-type spirals (Hubble type Sbc and earlier) a median value for p of 0.82 (in B-band). For her late-type spirals (Sc and later), she reports a median value of $p \sim 0.93$, which is more in agreement with the results we find for our fast rotators, although our sample is again closer to axisymmetry. This may not be so surprising though, given that the shape measurements of our sample of early-type galaxies do not suffer from additional structures introduced by spiral waves and dust, which are commonly present in spiral galaxies. Another possible explantion for the non-circularity of disc galaxies could come from lopsidedness (e.g. Rudnick & Rix 1998). We also compare our results with Padilla & Strauss (2008), who for their elliptical galaxies report $\mu_Y = -2.2 \pm 0.1, \mu_q = 0.43 \pm 0.06$ and for their spirals $\mu_Y = -2.33 \pm 0.13, \mu_q = 0.21 \pm 0.02$. Again, in comparison to both galaxy populations, our fast rotators are intrinsically closer to axisymmetry.

To check that our best-fit model is a reasonable fit to the data (and not simply the best of a set of only bad models), we plot in the bottom panel of Figure 13 the expected observed distribution $F(\Psi, \epsilon)$ given our best-fit $f(\mu_Y, \sigma_Y, \mu_q, \sigma_q)$, generated with Monte Carlo simulations, and we overplot the observed (Ψ, ϵ) values for our fast rotator galaxy sample. Errorbars have been omitted, but can be found in Paper II: the median error in ellipticity is 0.03, while the median error in kinematic misalignment is 6°. Apart from a few (mostly barred or interacting) outliers with high Ψ, the predicted distribution by our best-fit model closely follows the observed distribution.

Finally, we fit an intrinsic aligned model ($\theta_{\rm int} = 0$) to our data. In triaxial systems, alignment occurs when the long-axis tube orbits cancel each other out, or when the system is dominated by short-axis tube and box orbits instead. The observed kinematic misalignment therefore cannot originate from intrinsic misalignment, and has to be caused by projection of the triaxial intrinsic shape only (see Appendix A1, and in particular Equations A4-A6 for details). This model would therefore set a firm upper limit on the allowed amount of triaxiality in our galaxy population. We find again

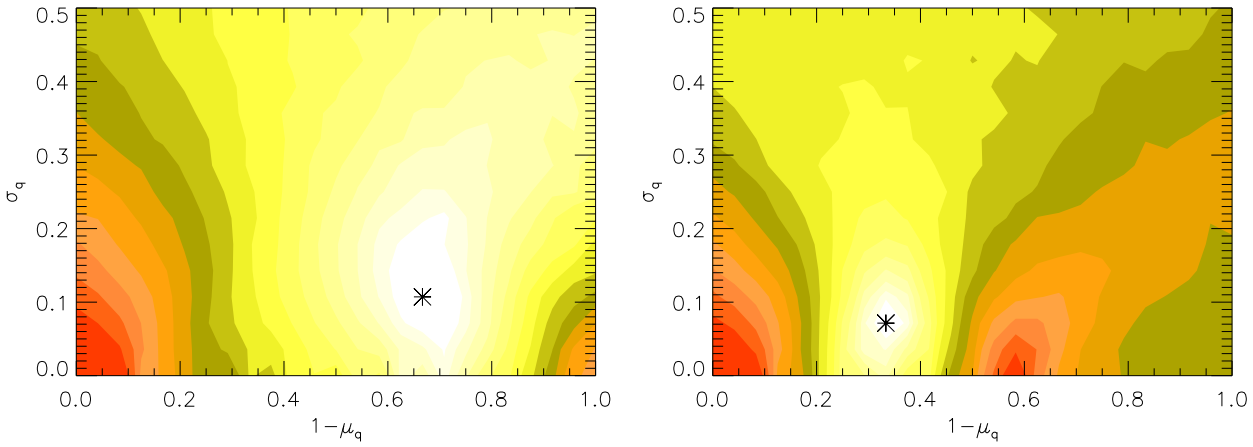

Figure 12. Contours of constant χ^2 assuming oblate intrinsic shapes with a Gaussian distribution in q for the fast rotator (left) and slow rotator (right) samples. Contours increase logarithmically from light to darker colours, and the minimal χ^2 value is indicated with a black asterisk.

a best fit for $\mu_Y = -5$ (or equivalently, $p \sim 0.99$), although with a larger best-fit standard-deviation $\sigma_Y = 0.42$. We therefore conclude that the fast rotators are indeed oblate systems, and that if there are any deviations from axisymmetry, these would have to be small.

Unfortunately, a similar analysis for the slow rotators in our sample failed due to the small sample size compared to the parameter space, as well as the lack of a clearly defined projected rotation axis in many of the systems (most notably for the non-rotators, or class *a* galaxies in our sample). Fixing the intrinsic flattening to $\mu_q = 0.66$ and $\sigma_q = 0.08$, as derived from the axisymmetric distributions, we find for the model with $\theta_{\rm int}$ a best-fit of $\mu_Y = -5.0$ and $\sigma_Y = 0.08$, which is an oblate shape. However, as we show in Figure 14, the minimum is not clearly defined, and the best-fit model is not able to reproduce the observed kinematic misalignment. We also note that a model with a larger triaxiality $\mu_Y = -3.0$ does allow for the larger observed misalignments, but does not reproduce the rounder observed shapes. The derived numbers are therefore not trustworthy. A model with no intrinsic misalignment ($\theta_{\rm int} = 0$) did prefer a triaxial model, but also did not show a clear minimum in χ^2, and also was not able to reproduce the observed distributions.

5 SUMMARY AND CONCLUSION

We inverted the observed ellipticity distributions of the early-type galaxies in the ATLAS^{3D} sample to obtain their intrinsic shapes. Based on kinematical classification, we divided our sample into fast and slow rotators, and inverted these populations separately. We find that the fast rotator population is significantly flatter than the slow rotator population ($\mu_q = 0.25$ versus $\mu_q = 0.63$, assuming axisymmetry), and that we cannot treat early-type galaxies as one single population, but that we need to consider fast and slow rotators separately. This is consistent with the conclusions in previous papers of this series: in Paper II we noted that based on their kinematic alignment, fast rotators are consistent with being axisymmetric, while slow rotators are not. In Papers III and VII we pointed out the difference in observed axial ratios between fast and slow rotators, while in Paper XVII we uncovered a distinction between fast and slow rotators in terms of the presence of discs from photometric decomposition. Finally, in Paper XX we showed dynamical models to deproject the galaxies, while in this paper we use a statistical inversion to show the difference in intrinsic flattening between fast and slow rotators. Given that both lenticular and elliptical galaxies are present in the fast rotator class, a purely morphological classification would not have been sufficient for the shape study presented in this paper.

We did not observe any trends of intrinsic shape with environment or stellar mass for the fast rotators, but we did note a decrease in observed ellipticity above stellar masses of $\sim 10^{11} M_\odot$ for the total early-type galaxy population, which is mainly driven by round massive, non-rotating slow rotators. We showed with simulations that our results are not affected by (weak) bars, which could potentially increase the observed ellipticity of their host galaxies.

Fast rotators have similar intrinsic flattening as spiral galaxies, which is in line with the results of Paper XVII, where we showed that fast rotators show a large span in disc-to-total ratios, and with the classification scheme introduced by Van den Bergh (1976), and revisited in Paper VII to emphasize the parallelism between fast rotators and spirals (see also Laurikainen et al. 2011; Kormendy & Bender 2012). This observation could hint to a similar evolutionary path of spirals and fast rotators, and it would be interesting to study this further in the context of the morphology-density relation, as mentioned in e.g. Paper VII, and Cappellari (2013c).

Next, we relaxed our assumption of axisymmetry and fitted triaxial models to our observations. We again took advantage of having integral-field data available for our dataset, by including the kinematic misalignment as an extra constraint in this fit. Assuming that the intrinsic misalignment is a function of intrinsic shape, we show convincingly that fast rotators are very close to oblateness, with only small deviations from axisymmetry allowed by our observations. Due to their small numbers in our sample, we could not repeat this analysis for the slow rotators, but based on their observed kinematic misalignment, we do expect this population to be more triaxial. That slow rotators are sys-

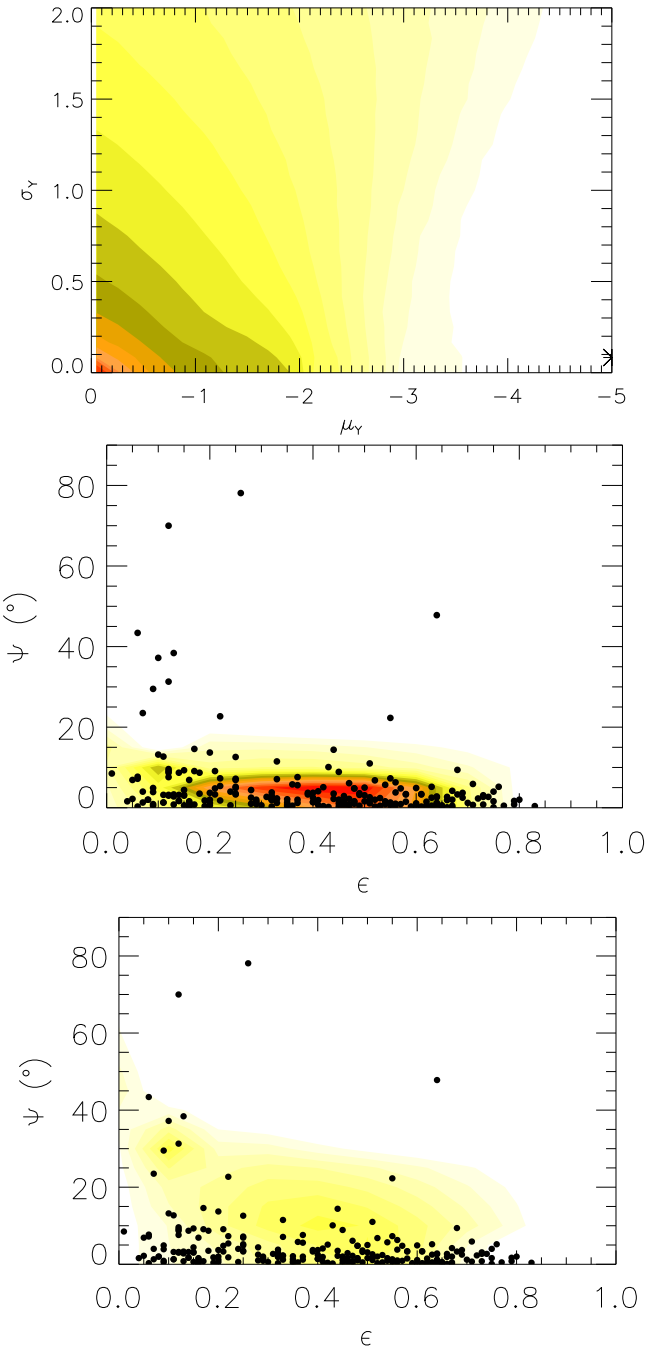

Figure 13. Top: contours of constant χ^2 for fast rotators as a function of μ_Y and σ_Y, assuming $\tan\theta_{\rm int} = \sqrt{T/(1-T)}$ and a Gaussian distribution in q, with parameters as indicated in the text. Contours are increasing logarithmically from light to dark colours, and the minimum in χ^2 is indicated with a black asterisk. Middle: contours indicate the distribution $F(\Psi, \epsilon)$, as predicted by the best-fit model indicated by the asterisk in the top panel. Contours increase linearly from light to dark colours. Overplotted in black dots is our observed fast rotator sample, indicating the nice agreement between model and observations. There are some galaxies with significant larger misalignment than predicted by our best-fitting model: these systems however all are dominated by strong bars or are interacting systems. Bottom: same as middle, but here we show a model with $\mu_Y = -3.0$. The corresponding distribution is overprediciting the number of galaxies with larger ($\Psi > 10°$) misalignment compared to the observations.

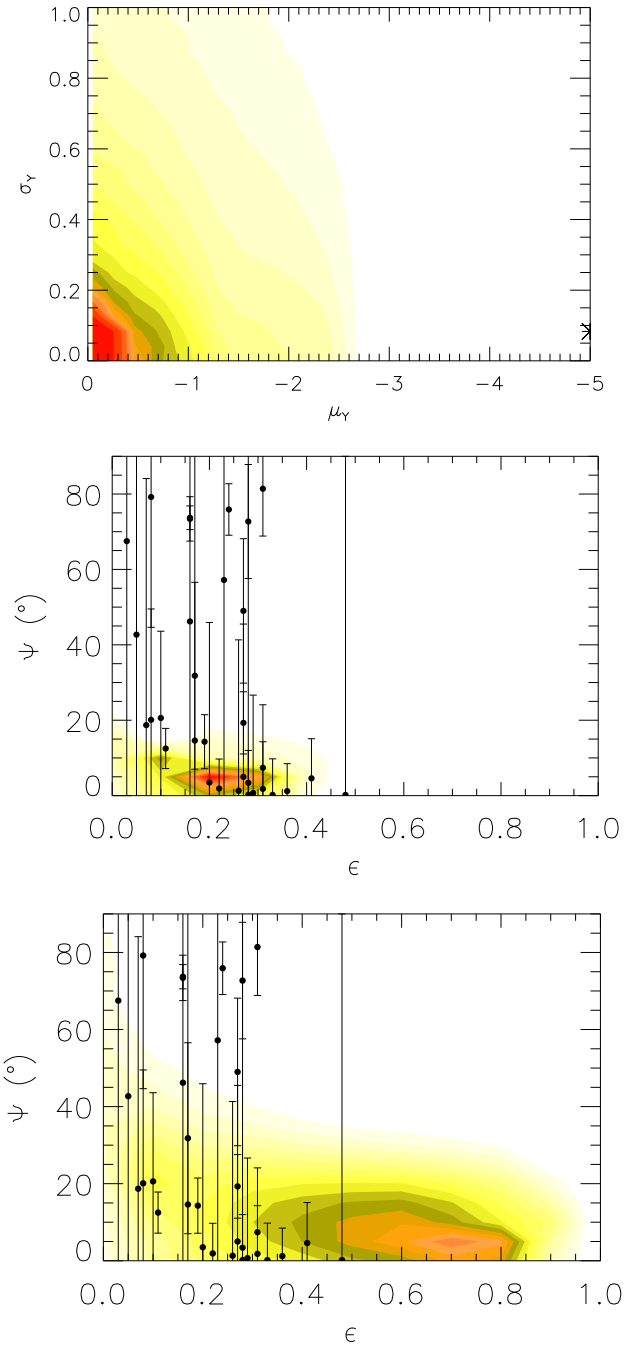

Figure 14. Same as Figure 13, but now for the slow rotators in our sample. Error bars have been added for Ψ, taken from Paper II. In the bottom plot we show again the predicted distribution for $\mu_Y = -3.0$. This model is too triaxial, as it overpredicts the number of flattened objects compared with the observations.

tematically rounder than fast rotators could also contribute to explain why, at a given mass, they appear to hold on better to their hot-gas medium and show brighter X-ray haloes (Sarzi et al. 2013, Paper XIX).

Despite the small size of the ATLAS^{3D} sample compared to the larger SDSS samples used in various previous shape studies, our sample has the big advantage of having kinematic information available. This not only allowed us to

separate the early-type galaxy populations in two distinct kinematical classes, which showed to have significantly different intrinsic shape distributions, but also made it possible to include the kinematic misalignment in our exploration of triaxial shape distributions. We therefore conclude that integral-field data is crucial to refine intrinsic shape studies, and to separate galaxy populations into distinct kinematical classes.

ACKNOWLEDGEMENTS

The authors thank Arjen van der Wel for kindly sharing his data, as well as fruitful discussions. The authors also thank the referee, for his/her constructive comments. This work was supported by the rolling grants Astrophysics at Oxford PP/E001114/1 and ST/H002456/1 and visitors grants PPA/V/S/2002/00553, PP/E001564/1 and ST/H504862/1 from the UK Research Councils. RLD acknowledges travel and computer grants from Christ Church, Oxford and support from the Royal Society in the form of a Wolfson Merit Award 502011.K502/jd. RLD is also grateful for support from the Australian Astronomical Observatory Distinguished Visitors programme, the ARC Centre of Excellence for All Sky Astrophysics, and the University of Sydney during a sabbatical visit. MC acknowledges support from a Royal Society University Research Fellowship. SK acknowledges support from the Royal Society Joint Projects Grant JP0869822. RMcD is supported by the Gemini Observatory, which is operated by the Association of Universities for Research in Astronomy, Inc., on behalf of the international Gemini partnership of Argentina, Australia, Brazil, Canada, Chile, the United Kingdom, and the United States of America. TN and MBois acknowledge support from the DFG Cluster of Excellence 'Origin and Structure of the Universe'. MS acknowledges support from a STFC Advanced Fellowship ST/F009186/1. PS acknowledges support of a NWO/Veni grant. TAD: The research leading to these results has received funding from the European Community's Seventh Framework Programme (/FP7/2007-2013/) under grant agreement No 229517. MBois has received, during this research, funding from the European Research Council under the Advanced Grant Program Num 267399-Momentum. LY acknowledges support from NSF AST-1109803. The authors acknowledge financial support from ESO. This paper is based on observations obtained at the William Herschel Telescope and the Isaac Newton Telescope, operated by the Isaac Newton Group in the Spanish Observatorio del Roque de los Muchachos of the Instituto de Astrofísica de Canarias. Funding for the SDSS and SDSS-II was provided by the Alfred P. Sloan Foundation, the Participating Institutions, the National Science Foundation, the U.S. Department of Energy, the National Aeronautics and Space Administration, the Japanese Monbukagakusho, the Max Planck Society, and the Higher Education Funding Council for England. The SDSS was managed by the Astrophysical Research Consortium for the Participating Institutions. This publication makes use of data products from the Wide-field Infrared Survey Explorer, which is a joint project of the University of California, Los Angeles, and the Jet Propulsion Laboratory/California Institute of Technology, funded by the National Aeronautics and Space Administration.

REFERENCES

Abazajian K.N., et al., 2009, ApJS, 182, 543
Arnold R., de Zeeuw P.T., Hunter C., 1994, MNRAS, 271, 924
Bacon R. et al., 2001, MNRAS, 326, 23
Binggeli B., 1980, A&A, 82, 289
Binney J., de Vaucouleurs G., 1981, MNRAS, 194, 679
Binney J., 1985, MNRAS, 212, 767
Blanton M.R., & Moustakas J, 2009, ARA&A, 47, 159
Bois M, et al., 2011, MNRAS, 416, 1654 (paper VI)
Cappellari M., 2002, A&A, 333, 400
Cappellari M., et al., 2007, MNRAS, 379, 418C
Cappellari M., et al., 2011a, MNRAS, 413, 813 (Paper I)
Cappellari M., et al., 2011b, MNRAS, 416, 1680 (Paper VII)
Cappellari M., et al., 2013a, MNRAS, 432, 1709 (Paper XV)
Cappellari M., et al., 2013b, MNRAS, 432, 1862 (Paper XX)
Cappellari M., 2013c, ApJL, 778, 2
Chang Y.-Y., et al., 2013, ApJ, 773, 149
Contopoulos G., 1956, Zeitschr. f. Astroph., 39, 126
Davis T.A., et al., 2014, MNRAS, in press (arXiv:1403.4850)
de Zeeuw P.T., Pfenniger D., 1988, MNRAS, 235, 949
de Zeeuw P.T., Franx M., 1989, ApJ, 343, 617
Emsellem E., et al., 2007, MNRAS, 379, 401
Emsellem E., et al., 2011, MNRAS, 414, 888 (Paper III)
Fasano G., Vio R., 1991, MNRAS, 249, 629
Franx M, 1988, MNRAS, 231, 285
Franx M., Illingworth G., de Zeeuw P.T., 1991, ApJ, 383, 112
Graham A.W., 2001, AJ, 121, 820
Holden B.P., van der Wel A., Rix H.-W., Franx M., 2012, ApJ, 749, 96
Hubble E.P., 1926, ApJ, 64, 321
Hunter C., de Zeeuw P.T., 1992, ApJ, 389, 79
Jarrett T.H., Chester T., Cutri R., Schneider S., Skrutskie M, Huchra J.P., 2000, AJ, 119, 2498
Jesseit R., Cappellari M., Naab T., Emsellem E., Burkert A., 2009, MNRAS, 397, 1202
Kimm T, Yi S.K., 2007, ApJ, 670, 1048
Kormendy J., Bender R., 2012, ApJS, 198, 2
Krajnović D., Cappellari M., de Zeeuw P.T., Copin Y., 2006, MNRAS, 366, 787
Krajnović D., et al., 2011, MNRAS, 414, 2939 (Paper II)
Krajnović D., et al., 2013, MNRAS, 432, 1768 (Paper XVII)
Lablanche P-Y, et al., 2012, MNRAS, 424, 1495 (Paper XII)
Lambas D.G., Maddox S.J., Loveday J., 1992, MNRAS, 258, 404
Landsman W.B., 1993, ASPC, 52, 246L
Laurikainen E., Salo H., Buta R., Knapen J.H., 2011, Advances in Astronomy, Vol 2011, 516739
Lucy L.B., 1974, AJ, 79, 745
Méndez-Abreu J., Simonneau E., Aguerri J.A.L, Corsini E.M., 2010, A&A, 521, 71
Padilla N.D., Strauss M.A., 2008, MNRAS, 388, 1321
Rudnick G., Rix H.-W., 1998, AJ, 116, 1163
Ryden B.S., 1996, ApJ, 461, 146
Ryden B.S., 2004, ApJ, 601, 214
Ryden B.S., 2006, ApJ, 641, 773
Sandage A., Freeman K.C., Stokes N.R., 1970, ApJ, 160, 831
Sarzi M., et al., 2013, MNRAS, 432, 1845 (Paper XIX)
Sérsic J.L., 1968, Altas de Galaxias Australes (Córdoba: Obs. Astron., Univ. Córdoba)
Scott N., et al., 2013, MNRAS, 432, 1894 (Paper XXI)
Statler T.S., 1994, ApJ, 425, 500
Statler T.S., Lambright H, Bak J., 2001, ApJ, 549, 871
Temi P., Brighenti F., Mathews W.G., 2009, ApJ, 707, 890
Tremblay B., Merrit D, 1996, AJ, 111, 2243
van den Bergh S., 1976, ApJ, 206, 883
van den Bosch R.C.E., van de Ven G., 2009, MNRAS, 398, 1117
van der Wel A., Rix H.-W., Holden B.P., Bell E.F., Robaina A.R., 2009, ApJ, 706L, 120

Vincent R.A., Ryden B.S., 2005, ApJ, 623, 137
Weinzirl T., Jogee S., Khochfar S., Burkert A., Kormendy J., 2009, ApJ, 696, 411
Wright E.L., et al., 2010, AJ, 140, 1868
Yuma S., Ohta K., Yabe K., 2012, ApJ, 761, 19

APPENDIX A: TRIAXIAL INTRINSIC SHAPE DISTRIBUTIONS

In this section we explore the triaxial shape distributions used in §4.4 in more detail. We first give the expression for ellipticity and kinematic misalignment as function of intrinsic axis ratio (p, q) and viewing angle (ϑ, φ) that were used to populate the simulated distributions, when we explored deviations from axisymmetry in our galaxy sample. We then give analytical expressions for the probability distributions $P(\Psi, \epsilon)$ and $P(\Psi)$, in the case of intrinsic misalignment coinciding with the viewing direction that yields an observed round galaxy (Equation 4), which is one of the assumptions we made in our triaxial analysis. We include these expressions here, as this case smoothly connects oblate models with the intrinsic rotation axis along the short axis (in agreement with their observed dynamics) with prolate models where the instrinsic rotation axis coincides with the long axis (again, in agreement with their observed dynamics). Many triaxial dynamical models therefore follow this relation. In addition, somewhat surprisingly given the need to calculate roots of polynomials, in this special case both the expressions $P(\Psi, \epsilon)$ and $P(\Psi)$ are elementary functions, and they were not previously recorded in Franx et al. (1991).

A1 Ellipticity and kinematic misalignment in triaxial systems

For oblate systems ($p = 1$), the observed ellipticity only depends on one viewing angle: the inclination ϑ (see Equation 1). For triaxial systems ($p \neq 1$) the observed ellipticity depends on both spherical viewing angles ϑ and φ (see also Figure 3, which shows observed ellipticity as function of viewing angle). The expression for ellipticity is then given by (e.g. Contopoulos 1956):

$$e = (1-\epsilon)^2 = \frac{a-\sqrt{b}}{a+\sqrt{b}}, \tag{A1}$$

with

$$\begin{aligned} a &= (1-q^2)\cos^2\vartheta + (1-p^2)\sin^2\vartheta\sin^2\varphi + p^2 + q^2, \\ b &= \left[(1-q^2)\cos^2\vartheta - (1-p^2)\sin^2\vartheta\sin^2\varphi - p^2 + q^2\right]^2 \\ &\quad + 4(1-p^2)(1-q^2)\sin^2\vartheta\cos^2\vartheta\sin^2\varphi. \end{aligned} \tag{A2}$$

For each triaxial shape there are four viewing directions that yield an observed ellipticity equal to zero (see right-hand panel in Figure 3); these viewing angles are given by $\vartheta = \theta_f, \pi - \theta_f$ and $\varphi = 0, \pi$, with θ_f given by:

$$\tan\theta_f = \sqrt{\frac{T}{1-T}}, \tag{A3}$$

and T the triaxiality parameter from Franx et al. (1991), as defined in Equation 5.

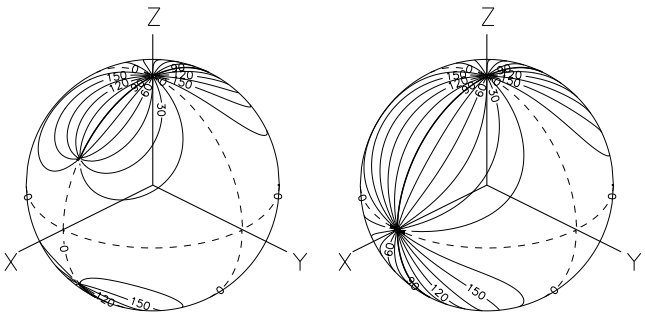

Figure A1. Contours of constant $\Theta_{\rm min}$ as given in Equation A6 on the sphere of viewing directions, defined by the angles (ϑ, φ). Left: $\tan\theta_f = \sqrt{2}$. Right: $\theta_f = \pi/2$. The dashed contour is for $\Theta_{\rm min} = 0$.

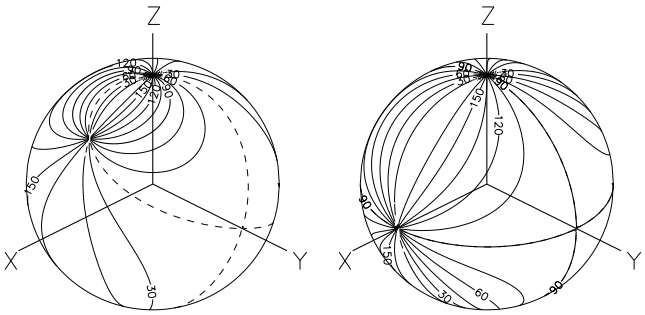

Figure A2. Contours of constant $\Theta_{\rm kin}$, defined in Equation (A5), on the sphere of viewing directions defined by the angles (ϑ, φ). Left: $\theta_{\rm int} = \pi/4$. Right: $\theta_{\rm int} = \pi/2$. While in the latter case all octants are similar, in the former case two distinct sets of octants occur. The dashed contour indicates $\Theta_{\rm kin} = \pi/2$.

Kinematic misalignment is the difference between the projected rotation axis $\Theta_{\rm kin}$ and the projected short axis $\Theta_{\rm min}$, and therefore defined as (e.g. Franx et al. 1991):

$$\sin\Psi = |\sin(\Theta_{\rm kin} - \Theta_{\rm min})|, \quad 0^\circ \leqslant \Psi \leqslant 90^\circ. \tag{A4}$$

$\Theta_{\rm kin}$ is a function of the viewing angles as well as the intrinsic misalignment $\theta_{\rm int}$. Measured with respect to the projected short axis, $\Theta_{\rm kin}$ can be calculated with a projection matrix (e.g. de Zeeuw & Franx 1989):

$$\tan\Theta_{\rm kin} = \frac{\sin\varphi\tan\theta_{\rm int}}{\sin\vartheta - \cos\varphi\cos\vartheta\tan\theta_{\rm int}}. \tag{A5}$$

$\Theta_{\rm min}$ depends on the intrinsic shape of the galaxy through the triaxiality parameter T as defined in Equation 5, and the viewing angles:

$$\tan 2\Theta_{\rm min} = \frac{2T\sin\varphi\cos\varphi\cos\vartheta}{\sin^2\vartheta - T(\cos^2\varphi - \sin^2\varphi\cos^2\vartheta)}. \tag{A6}$$

Examples of $\Theta_{\rm min}$, $\Theta_{\rm kin}$ and Ψ on the sphere of viewing angles are given in Figures A1, A2 and A3, respectively.

A2 Probability distributions $P(\Psi, \epsilon)$ for $\theta_{\rm int} = \theta_f$

Franx et al. (1991) presented in their appendix probability distributions $P(\Psi, \epsilon)$ for perfectly aligned triaxial systems, or $\theta_{\rm int} = 0$. By following their analysis and integrating over the sphere of viewing angles, we here give expressions for

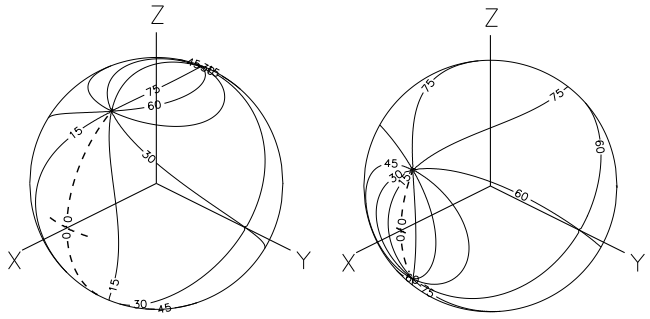

Figure A3. Contours of constant misalignment angle Ψ, defined in Equation A4, on the sphere of viewing directions defined by the angles (ϑ, φ). In both cases the model has intrinsic misalignment $\theta_{\rm int} = \theta_f$. Left: $T = 1/4$, or $\theta_{\rm int} = \pi/6$. Right: $T = 3/4$, or $\theta_{\rm int} = \pi/3$. The dashed contour corresponds to $\Psi = 0$.

$P(\Psi, \epsilon)$ with $\theta_{\rm int} = \theta_f$, with θ_f corresponding to the viewing direction from which the galaxy will appear round ($\epsilon = 0$), as defined in Equation A3.

We define $P(\vartheta, \varphi)\mathrm{d}\vartheta\mathrm{d}\varphi$ as the probability of finding ϑ and φ in the ranges $(\vartheta, \vartheta + \mathrm{d}\vartheta)$ and $(\varphi, \varphi + \mathrm{d}\varphi)$, respectively. Then $P(\vartheta, \varphi)$ is equal to the area element on the sphere of viewing angles, divided by the total area of the sphere, and hence is given by:

$$P(\vartheta, \varphi) = \frac{\sin\vartheta}{4\pi}. \tag{A7}$$

Therefore, it follows that:

$$P(\Psi, \epsilon)\,\mathrm{d}\Psi\mathrm{d}\epsilon = \sum_{(\vartheta_i, \varphi_i)} \frac{\sin\vartheta}{4\pi} \left| \frac{\partial(\Psi, \epsilon)}{\partial(\vartheta, \varphi)} \right|^{-1} \mathrm{d}\Psi\mathrm{d}\epsilon, \tag{A8}$$

where the sum is over all pairs of angles (ϑ_i, φ_i) with $0 \leqslant \vartheta_i \leqslant \pi$ and $0 \leqslant \varphi_i \leqslant 2\pi$ for which $\Psi(\vartheta, \varphi) = \Psi$ and $\epsilon(\vartheta, \varphi) = \epsilon$). [5]

Franx (1988) showed that the properties of projected triaxial ellipsoids are more effectively described in terms of conical coordinates (μ, ν) instead of spherical coordinates (ϑ, φ), so we continue our analysis in this coordinate system instead. The relation between conical and spherical coordinates is given by (e.g. de Zeeuw & Pfenniger 1988, their Equations 5.4-5.6):

$$\begin{aligned} \cos^2\vartheta &= \frac{(\mu - q^2)(\nu - q^2)}{(1 - q^2)(p^2 - q^2)}, \\ \tan^2\varphi &= \frac{(\mu - p^2)(p^2 - \nu)(1 - q^2)}{(1 - \mu)(1 - \nu)(p^2 - q^2)}, \end{aligned} \tag{A9}$$

such that each combination (μ, ν) corresponds to eight directions, given by $(\vartheta, \pm\varphi)$, $(\vartheta, \pm[\pi - \varphi])$, $(\pi - \vartheta, \pm\varphi)$ and $(\pi - \vartheta, \pm[\pi - \varphi])$. The area element $\mathrm{d}\Omega = \sin\theta\mathrm{d}\vartheta\mathrm{d}\varphi$ on the unit sphere is given by:

$$\mathrm{d}\Omega = \frac{(\mu - \nu)\mathrm{d}\mu\mathrm{d}\nu}{4\sqrt{-h(\mu)}\sqrt{h(\nu)}}, \tag{A10}$$

with

$$h(\tau) = (\tau - 1)(\tau - p^2)(\tau - q^2). \tag{A11}$$

Combining Equations A7 and A10, it then follows that the probability of finding μ and ν on the sphere of viewing angles in the ranges $(\mu, \mu + \mathrm{d}\mu)$ and $(\nu, \nu + \mathrm{d}\nu)$, respectively, is equal to:

$$P(\mu, \nu) = \frac{(\mu - \nu)}{16\pi\sqrt{-h(\mu)}\sqrt{h(\nu)}}, \tag{A12}$$

such that

$$P(\Psi, \epsilon)\mathrm{d}\Psi\mathrm{d}\epsilon = \sum_{\mu_i, \nu_i} P(\mu, \nu) \left| \frac{\partial(\mu, \nu)}{\partial(\Psi, \epsilon)} \right| \mathrm{d}\Psi\mathrm{d}\epsilon, \tag{A13}$$

where μ_i and ν_i are all the pairs of solutions of $\Psi(\mu, \nu) = \Psi$ and $\epsilon(\mu, \nu) = \epsilon$.

To continue, we have to know expressions for our observables ϵ and Ψ similar to Equations A1 and A4, but now in conical coordinates μ, ν. For ϵ, we combine Equations A1, A2 and A9 to arrive at (see also de Zeeuw & Pfenniger 1988, their Equation 5.4):

$$\epsilon = 1 - \sqrt{\frac{\nu}{\mu}}, \quad \text{or} \quad e = \frac{\nu}{\mu}. \tag{A14}$$

For Ψ, it can be shown by combining Equations A4, A5, A6 and A9 that:

$$\tan\Psi = \frac{(R_1 \mp AR_2)\sqrt{\mu - p^2}}{(R_2 \mp AR_1)\sqrt{p^2 - \nu}}, \tag{A15}$$

where we have defined the auxiliary functions

$$R_1 = \sqrt{(1 - \mu)(\nu - q^2)}, \quad R_2 = \sqrt{(\mu - q^2)(1 - \nu)}, \tag{A16}$$

and

$$A = \sqrt{\frac{1 - T}{T}}\tan\theta_{\rm int}. \tag{A17}$$

Note that for the case that we are studying $\theta_{\rm int} = \theta_f$, and therefore $A = 1$. We now introduce $t = \tan\Psi$, such that:

$$\mathrm{d}\Psi = \frac{\mathrm{d}t^2}{2t(1 + t^2)}, \tag{A18}$$

and therefore:

$$\left| \frac{\partial(\mu, \nu)}{\partial(\Psi, \epsilon)} \right|^{-1} = \frac{1}{4t(1+t^2)\,\mu^{3/2}\nu^{1/2}} \left| \mu\frac{\partial t^2}{\partial\mu} + \nu\frac{\partial t^2}{\partial\nu} \right|. \tag{A19}$$

We simply the above expression by substituting $\nu = e\mu$ (Equation A14), and combining the result with Equation A13, we arrive at:

$$P(\Psi, \epsilon) = \sum_i \frac{(1-e)\sqrt{e}\,t(1+t^2)\,\mu_i^2}{4\pi\sqrt{-h(\mu_i)h(e\mu_i)}} \left| \frac{\mathrm{d}t^2}{\mathrm{d}\mu} \right|^{-1}_{\mu=\mu_i}, \tag{A20}$$

where the sum is over all octants, and over all physical roots $p^2 \leqslant \mu_i \leqslant 1$ of the equation $t^2(\mu_i, e\mu_i) = t^2$, and $h(\mu)$ is defined in Equation A11.

We now concentrate on the case $\theta_{\rm int} = \theta_f$, and the expressions for t^2 and $|\mathrm{d}t^2/\mathrm{d}\mu|$ simplify to (see Equations A15 - A17:

$$t^2 = \frac{\mu - p^2}{p^2 - e\mu}, \qquad \frac{\mathrm{d}t^2}{\mathrm{d}\mu} = \frac{(1 - e)p^2}{(p^2 - e\mu)^2}, \tag{A21}$$

[5] Equation (A24) of Franx et al. (1991) erroneously replaces $\sin\vartheta$ by $\cos\vartheta$. This is a typographical error with no impact on their equations (A25)–(A29).

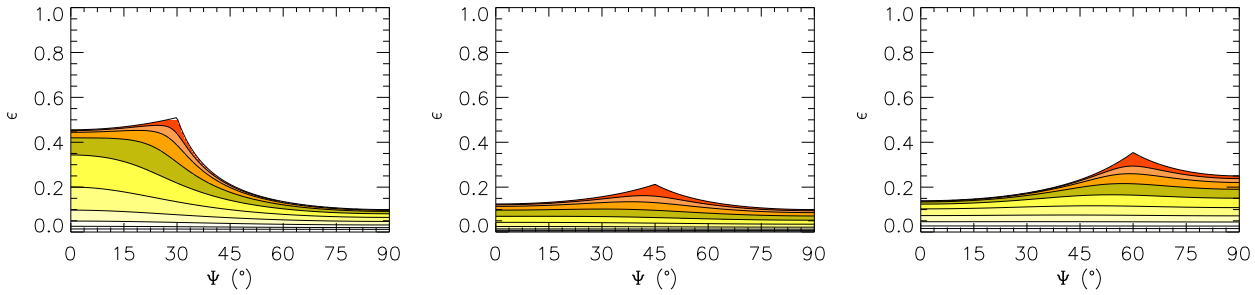

Figure A4. Probability distributions $P(\Psi,\epsilon)$ for $\theta_{\rm int}=\theta_f$. Left: $\theta_{\rm int}=30°$, $p=0.9$. Middle: $\theta_{\rm int}=45°$, $p=0.9$. Right: $\theta_{\rm int}=60°$, $p=0.75$. The triaxiality increases in these plots from $T=0.25$ (left), $T=0.50$ (middle) to $T=0.75$ (right). Contours are spaced logarithmically and increase with darker colours. $P(\Psi,\epsilon)$ is singular on the boundary curves.

which is valid in all octants. Solving for μ using the left-hand expression in Equation A21 results in a single root μ_1 contributing to $P(\Psi,\epsilon)$:

$$\mu_1=\frac{p^2(1+t^2)}{(1+et^2)}=\frac{p^2}{\cos^2\Psi+e\sin^2\Psi}. \qquad \text{(A22)}$$

Substituting this root μ_1 into Equation A20 then leads us finally to an expression for the probability distribution $P(\Psi,\epsilon)$ with $\theta_{\rm int}=\theta_f$:

$$P(\Psi,\epsilon)=\frac{2(1-e)\sqrt{e}\,\mu_1^3}{\pi p^2\sqrt{1-\mu_1}\sqrt{e\mu_1-q^2}\sqrt{1-e\mu_1}\sqrt{\mu_1-q^2}}. \qquad \text{(A23)}$$

The area in the (Ψ,ϵ)-plane where $P(\Psi,\epsilon)$ is non-zero is bounded by $\epsilon=0$, $\Psi=0$, $\Psi=\pi/2$, and two boundary curves, $e=e_{\rm I}(\Psi)$ and $e=e_{\rm II}(\Psi)$ with

$$\begin{aligned} e_{\rm I} &= \frac{q^2}{p^2+(p^2-q^2)t^2}, \qquad (0\leqslant\Psi\leqslant\theta_f),\\ e_{\rm II} &= p^2-\frac{(1-p^2)}{t^2}, \qquad (\theta_f\leqslant\Psi\leqslant\tfrac{\pi}{2}). \end{aligned} \qquad \text{(A24)}$$

$P(\Psi,\epsilon)$ diverges on both these curves, which join at $e=q^2$ and $\Psi=\theta_{\rm int}=\theta_f$. $P(\Psi,\epsilon)$ vanishes in the limit $\epsilon\downarrow 0$, but is finite for $\Psi=0$ and $\pi/2$. In Figure A4 we show several examples of $P(\Psi,\epsilon)$.

A2.1 $P(\Psi)$ for $\theta_{\rm int}=\theta_f$

For completeness, we also derive the probability distribution $P(\Psi)$ for the case that $\theta_{\rm int}=\theta_f$. This expression can be obtained by integrating $P(\Psi,\epsilon)$ as given in Equation A20 over $\mathrm{d}\epsilon=\mathrm{d}e/2\sqrt{e}$, which results in:

$$P(\Psi)=\frac{t(1+t^2)}{8\pi}\sum_i\int_{e_-}^{e_+}\mathrm{d}e\,\frac{(1-e)\mu_i^2}{\sqrt{-h(\mu_i)h(e\mu_i)}}\left|\frac{\mathrm{d}t^2}{\mathrm{d}\mu}\right|^{-1}_{\mu=\mu_i}, \qquad \text{(A25)}$$

where the sum is taken over all octants, and all physical roots $p^2\leqslant\mu_i\leqslant 1$ of $t^2(\mu_i,e\mu_i)=t^2$. The integration limits e_- and e_+ depend on p, q and $\theta_{\rm int}$. For our purposes, it is convenient to substitute μ back for e into this equation, leading to:

$$P(\Psi)=\frac{t(1+t^2)}{8\pi}\sum_i\int_{\mu^-}^{\mu^+}\mathrm{d}\mu\,\frac{(\mu-\nu_i)}{\sqrt{-h(\mu)h(\nu_i)}}\left|\frac{\mathrm{d}t^2}{\mathrm{d}\nu}\right|^{-1}_{\nu=\nu_i}, \qquad \text{(A26)}$$

where the sum is over all octants, and $q^2\leqslant\nu_i(\mu,t^2)\leqslant p^2$ is a root of $t^2(\mu,\nu)=t^2$. This expression can also be derived directly from the fundamental probability distribution (A12) by the transformation $(\mu,\nu)\rightarrow(\mu,\Psi)$, and has the advantage that all quantities are functions of T only, which is not the case for expression (A25) which contains e.

It further is useful to transform from (μ,ν) to the rescaled conical coordinates $(\bar\mu,\bar\nu)$, defined as:

$$\bar\mu=\frac{\mu-p^2}{1-q^2}, \qquad \bar\nu=\frac{\nu-p^2}{1-q^2}, \qquad \text{(A27)}$$

so that $\bar\mu\geqslant 0$ and $\bar\nu\leqslant 0$. Substituting these coordinates in Equation A26 and taking the sum over all eight octants then leads to the simplified expression

$$P(\Psi)=\frac{t(1+t^2)}{\pi}\sum_i\int_0^{\bar\mu^+}\frac{\mathrm{d}\bar\mu\,(\bar\mu-\bar\nu)}{\sqrt{-\bar h(\bar\mu)\bar h(\bar\nu)}}\left|\frac{\mathrm{d}t^2}{\mathrm{d}\bar\nu}\right|^{-1}_{\bar\nu=\bar\nu_i}, \qquad \text{(A28)}$$

where $\bar\nu_i=\bar\nu_i(\bar\mu)$ are all solutions of $t^2(\bar\mu,\bar\nu)=0$ in the interval $-(1-T)\leqslant\bar\nu\leqslant 0$, and

$$\bar h(\bar\tau)=\bar\tau(T-\bar\tau)(\bar\tau+1-T). \qquad \text{(A29)}$$

We now express Equation A21 in terms of $\bar\mu$ and $\bar\nu$ as given by Equation A27, to arrive at:

$$t^2=-\frac{\bar\mu}{\bar\nu}, \qquad \frac{\mathrm{d}t^2}{\mathrm{d}\nu}=-\frac{t^2}{\bar\nu}, \qquad \text{(A30)}$$

Substituting the above expressions into Equation A28, we finally obtain:

$$P(\Psi)=\frac{(1+t^2)^2}{\pi t^2}\begin{cases}\displaystyle\int_0^{(1-T)t^2}\frac{\bar\mu\mathrm{d}\bar\mu}{\sqrt{P_4(\bar\mu)}}, & (0\leqslant t^2\leqslant\frac{T}{1-T}),\\[2ex] \displaystyle\int_0^{T}\frac{\bar\mu\mathrm{d}\bar\mu}{\sqrt{P_4(\bar\mu)}}, & (\frac{T}{1-T}\leqslant t^2),\end{cases} \qquad \text{(A31)}$$

where P_4 is a polynomial of degree 4 in $\bar\mu$, given by

$$P_4(\bar\mu)=(T-\bar\mu)(\bar\mu+1-T)([1-T]t^2-\bar\mu)(\bar\mu+Tt^2). \qquad \text{(A32)}$$

It can be shown that:

$$P(\Psi;T)=P(\tfrac{\pi}{2}-\Psi;1-T), \qquad \text{(A33)}$$

so that we need to evaluate $P(\Psi;T)$ only for $0\leqslant T\leqslant 1/2$.

$P(\Psi)$ can be expressed in terms of incomplete elliptic integrals. It diverges logarithmically for $\Psi=\theta_{\rm int}$, and is

Table A1. Special values of $P(\Psi)$ for the case where $\theta_{\rm int} = \theta_f$.

Ψ	$P(\Psi)$
0	$\frac{1}{\pi} - \frac{(2T-1)}{\pi\sqrt{T(1-T)}} \arctan\sqrt{\frac{1-T}{T}}$
$\frac{\pi}{2} - \theta_{\rm int}$	$\frac{1}{\pi}\left\{\frac{[\sqrt{T(1-T)}-1]}{T(1-T)} \ln(1-2T) - \ln(\sqrt{T}+\sqrt{1-T})\right\}$
$\frac{\pi}{2}$	$\frac{1}{\pi} - \frac{(1-2T)}{\pi\sqrt{T(1-T)}} \arctan\sqrt{\frac{T}{1-T}}$

elementary for $\Psi = 0$, $\pi/2 - \theta_{\rm int}$, and $\pi/2$. The expressions for these special cases are given in Table A1.

The entire function $P(\Psi)$ is elementary for $T = 1/2$, and is given by

$$P(\Psi; 1/2) = -\frac{2\ln|\cos 2\Psi|}{\pi \sin^2 2\Psi}, \tag{A34}$$

which satisfies $P(\Psi) = P(\frac{\pi}{2} - \Psi)$. It follows that $P(0; 1/2) = P(\pi/2; 1/2) = 1/\pi$, and $P(\Psi; 1/2)$ diverges logarithmically at $\Psi = \pi/4$. In this case the cumulative distribution is elementary as well. It is given by

$$\bar{P}(\Psi) = \frac{1}{2} + \frac{\ln|\cos 2\Psi|}{\pi \tan 2\Psi} - \frac{\arcsin(\cos 2\Psi)}{\pi}. \tag{A35}$$

This equals 1/2 when $\Psi = \pi/4$, in accord with the symmetric nature of $P(\Psi)$.

APPENDIX B: KINEMATIC MISALIGNMENT AS SOLE SHAPE TRACER

As derived in the previous section, observed kinematic misalignment Ψ depends on the intrinsic rotation misalignment $\theta_{\rm int}$ and the intrinsic shape of a galaxy. The dependence on intrinsic shape is solely given by the triaxiality T of the system, and as such, we could try to infer the intrinsic shape distribution of our galaxy sample from the observed misalignement distribution, parametrising the intrinsic shape with T only. As we did before with the observed histogram of ellipticity, we now approximate the observed histrogram of kinematic misalignment (Figure 2) with a sum of Gaussians, whose standard deviation is given by the measurement errors. We mirror the resulting distribution around $\Psi = 90^\circ$. As a clear rotation axis is not always easy to identify for the slow rotators, the measurement errors for individual galaxies are rather large (up to 90°), resulting in a rather flat distribution of kinematic misalignment.

We first assume that the intrinsic misalignment is zero ($\theta_{\rm int} = 0$). This is not a very realistic assumption as especially highly triaxial models are expected to display significant intrinsic misalignment, but does showcase the maximum allowed triaxiality, as intrinsic misalignment does not contribute to the observed kinematic misalignment (see Equation A4). Generating model galaxies with random viewing angles using Monte Carlo simulations, and binning the observed and simulated samples in bins of 5°, we find with a simple χ^2 fit that the best-fitting intrinsic shape for the slow rotators would have a triaxiality of $T = 1$, which corresponds to a prolate shape. As prolate galaxies are extremely rare in our sample, and previous analyses have shown that the slow rotators in our sample are only mildy triaxial (e.g. Paper III), we cannot take this result at face value. Similarly, the fast rotator sample is best fitted with a shape distribution of $T = 0.45$, which is unrealistically high. This best-fitting value goes down to $T = 0.35$ if we exclude galaxies that are barred or interacting (Paper II). We show the resulting fits in Figure B1, with solid coloured lines.

A more realistic model would be to allow the intrinsic misalignment to increase with increasing triaxiality, by assuming as before that $\theta_{\rm int} = \theta_{\rm f}$ (see Equation A3). We then obtain a best-fitting distribution $T = 0.25$ for the slow rotator sample, and $T = 0.05$ for the fast rotator sample. This last value does not change when excluding barred and interacting systems. We show these fits too in Figure B1, with dashed lines. Although these values seem more realistic, the fits are worse than for the model with no intrinsic misalignment. The results of this analysis show that kinematic misalignment alone is not a good tracer of intrinsic shape. The probability distribution $P(\Psi)$ strongly depends on the intrinsic misalignment in the model: it has a singularity for $\Psi = \theta_{\rm int}$, as shown in e.g. figure 9a of Franx et al. (1991). The triaxiality T in contrast has a much milder influence on $P(\Psi)$ (e.g. figure 5a of Franx et al. 1991). We therefore warn against over-interpreting this simple analysis, as valuable information on the shapes of galaxies (their ellipticities) has not been used: indeed, this exercise shows the importance of including both shape and misalignment information when recovering intrinsic shape distributions. We refer the reader to the results presented in the main body of this paper as more reliable representations of the intrinsic shapes.

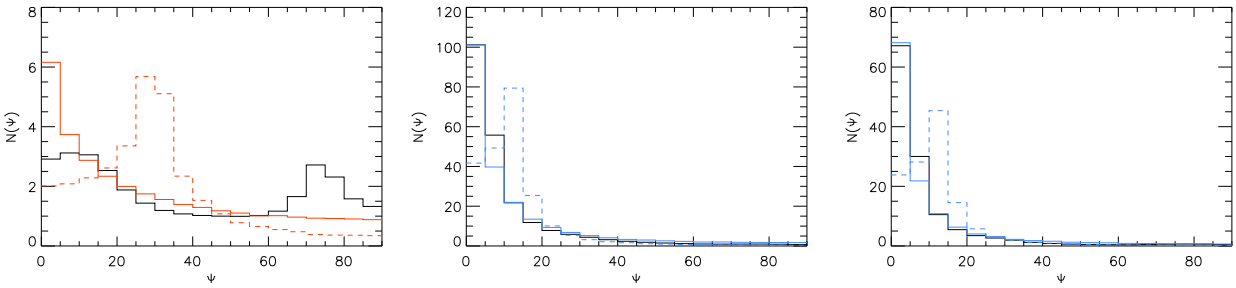

Figure B1. Observed distributions of kinematic misalignment (black histogram), constructed from Gaussians representing individual galaxies and their measurement errors (see text for detail). From left to right we show the slow rotators, fast rotators, and a 'clean' sample of fast rotators excluding barred and interacting galaxies. Overplotted we show best-fit models assuming constant triaxiality and no intrinsic misalignment (solid coloured lines) or intrinsic misalignment scaling with triaxiality as $\theta_{\rm int} = \theta_{\rm f}$ (dashed coloured lines). The intrinsically aligned models give by eye a good fit to the observed kinematic misalignment distributions, but yield unrealistically high triaxiality values ($T = 1.0$, 0.45 and 0.35 for the slow rotators, fast rotators, and clean sample, respectively).